CHALMERS

DIPLOMA WORK 03/15

Modeling of Swirling Flow in a Conical Diffuser

WALTER GYLLENRAM

Division of Thermo and Fluid Dynamics
CHALMERS UNIVERSITY OF TECHNOLOGY
Göteborg, Sweden 2003

Modeling of Swirling Flow in a Conical Diffuser
Walter Gyllenram
©Walter Gyllenram 2003

Division of Thermo and Fluid Dynamics
CHALMERS UNIVERSITY OF TECHNOLOGY
SE-412 96 Göteborg, Sweden
Phone +46-(0)31-7721400
Fax +46-(0)31-180976

Abstract

This work aims at getting a better understanding of the turbulent swirling flow in a conical diffuser, which represents a highly simplified draft tube of a water turbine. The numerical 3D (U)RANS investigations are quantitatively compared to experimental data. Qualitative comparison with experimental visualizations and computations of similar flows are also made, and strong similarities to confined swirling flow have been found. Converging/diverging smearlines at the walls reveal a very complex boundary layer and counter-rotating vortex structures are found at the diffuser exit. The solutions to the Reynolds averaged Navier-Stokes equations for the studied cases are asymmetric. The asymmetry of the mean flow solution is originating from instable properties of the symmetric mode, and the disturbance that triggers the instability is proven to be imperfections of the CAD-geometry.

There are some discrepancies regarding the agreements with experimental data, partly reminiscent of the nature of the $(k-\omega)$ turbulence model that was used in this work. The origins of turbulent anisotropy are theoretically examined as well as the weaknesses of the Boussinesq assumption, which constitutes an important part of the chosen turbulence model.

Also included are a discussion concerning the origin of turbulent anisotropy and aspects of the filtered (LES) and the averaged (RANS) equations.

Preface

This work will serve as a step towards a better understanding of hydraulic turbine draft tube flow, since the diffuser that constitutes the computational domain of this work can be considered a highly simplified draft tube. In the first chapter the role of the diffuser in the context of hydroelectric power generation is discussed. In chapter 2 the governing equations of fluid motion are introduced, followed by the numerical considerations and the results in chapter 3 and 4 respectively. The subsequent chapters includes conclusions and some notes of future work. A theoretical discussion concerning the expected behavior of turbulence in swirling flow through a diffuser are included in appendix, as well as a few words on the aspects of averaging the governing equations.

Acknowledgments

I would like to thank Dr. Ole Gunnar Dahlhaug of NTNU, Trondheim, Norway, for providing the experimental data that are used in this work and my supervisor, Dr. Håkan Nilsson, for his support during the project.

This work was financially supported by ELFORSK (Swedish Electrical Utilities Research and Development Company), the Swedish National Energy Administration and GE Energy (Sweden) AB.

Nomenclature

Roman

A	Area
C_p	Pressure rise coefficient
k	Turbulent kinetic energy
L	Length
N_{CFL}	Courant-Friedrichs-Levy (CFL) number, $\frac{u\Delta t}{\Delta x}$
P, p	Static pressure
P_0	Stagnation pressure
P_k	Production term in k-equation
P_k^{model}	Modeled production term
q	Volume flow
R	Radius
Re	Reynolds number, $\frac{UL}{\nu}$
S	Swirl intensity
T	Time
$\mathbf{u}$, u_i	Velocity vector/tensor
U, V, W	Mean velocity components
u', v', w'	Fluctuating components of velocity vector
y^+	Dimensionless wall normal distance, $\frac{u^* y_n}{\nu}$

Greek

Δ	Length scale of computional cell
ε	Dissipation
θ	Angle
μ	Dynamic viscosity
ν	Kinematic viscosity
ν_t	Turbulent viscosity
ρ	Density
τ_w	Wall friction
φ	Helicity, $\frac{\omega_i u_i}{\lvert\omega_i\rvert\lvert u_i\rvert}$
ω	Specific dissipation
ω	Vorticity vector, $\nabla \times \mathbf{u}$

Symbols

$<(\cdot)>$	Ensemble average
$\overline{(\cdot)}$	Time average
$\widehat{(\cdot)}$	Spatial or time filter

Super- and Subscripts

B, C, D, E, F	Cross-section
$axial$	Axial direction
$calc$	Calculated
cl	Centerline
cr	Cross-sectional
exp	Experimental
i, j, k	Principal direction
m	Mixing (length)
p	Pressure
R	Ratio
rad	Radial direction
sgs	Subgrid scale
tan	Tangential direction
x, y, z, r, θ	Direction in space
1, 2	Inlet, outlet

Abbreviations

CFD	Computational Fluid Dynamics
CFL	Courant, Friedrichs, Lewy (number)
DNS	Direct Numerical Simulation
FVM	Finite Volume Method
HRN	High Reynolds Number (model)
LES	Large Eddy Simulation
LRN	Low Reynolds Number (model)
MPI	Messege Passing Interface
RANS	Reynolds Averaged Navier-Stokes (equations)
RSM	Reynolds Stress Model
TDMA	Tri-Diagonal Matrix Algorithm
URANS	Unsteady Reynolds Averaged Navier-Stokes (equations)
PDE	Partial Differential Equation
PIV	Particle Image Velocimetry

Contents

Abstract iii

Preface v

Acknowledgements vii

Nomenclature xi

1 Introduction 1
- 1.1 Hydroelectric Power 1
- 1.2 The Draft Tube 3
- 1.3 Some Implications of Swirling Flow 4
- 1.4 Methods and Software 5
- 1.5 The Experimental Data 6

2 Governing Equations 7
- 2.1 Equations of Motion 7
- 2.2 The Averaged Equations - RANS 7
- 2.3 Reynolds Stress Equation 8
- 2.4 Turbulent Kinetic Energy Equation 9
- 2.5 Filtered Equations and the LES 10

3 Numerical Procedure 13
- 3.1 The System of Equations 14
- 3.2 The Computational Domain 14
- 3.3 Boundary Conditions 14
- 3.4 The Grids 16

4 Results and Discussion 19
- 4.1 Vortex Structures and Boundary Layer Interaction 19
- 4.2 The Pressure Distribution 21
- 4.3 The Mean Velocity Profiles 21

4.4 The Turbulent Quantities 22
4.5 Instability of the Symmetric Mode 23
4.5.1 Spontaneous and Forced Symmetry Breaking 24
4.5.2 A Search for the Disturbance 25

5 Conclusions 37

6 Future Work 39

Appendix 41

A A Return to the Equations 41
A.1 The Influence of Swirl on Turbulence 41
A.2 The Influence of the Diffuser on Turbulence 43
A.3 The Axial Pressure Gradient 44

B Some Notes on Averaging 47
B.1 Why Average? 47
B.1.1 Physical Instability - Numerical Stability 47
B.2 Aspects of Averaging 48
B.2.1 RANS 48
B.2.2 URANS 49
B.2.3 The Ensemble Average and the Randomness of Turbulence 50
B.2.4 Filtered Functions and the LES 50

C The Most Common Turbulence Models 53
C.1 The $k - \varepsilon$ Model 53
C.2 The $k - \omega$ Model 54
C.3 The Reynolds Stress Model 55
C.4 Limitations of the Boussinesq Assumption 56

Bibliography 60

Chapter 1

Introduction

About 50 % of the electrical power produced in Sweden are generated by water turbines. Consequently, even a small improvement of the hydrodynamic design can contribute a great deal to the supply of electric power. In this chapter, a few issues concerning the hydrodynamic aspects of the flow through a water turbine are discussed, in order to elucidate the intentions of this work.

1.1 Hydroelectric Power

Water turbines are designed to extract energy from water. The potential energy of water is proportional to the (static) head and by letting gravity work on the water, the potential energy is converted to kinetic energy. This energy is in turn converted to electrical energy by leading the water through a runner, connected to a generator (see figure 1.1.1). Depending on the head, different types of turbines are used. As examples of two different types, the Francis turbine[1] and the Kaplan turbine can be mentioned. The latter was developed by the Austrian engineer Victor Kaplan (1876-1934). At heads ranging from 40 to 700 m, Francis turbines are usually preferred. Kaplan turbines are used at heads up to 60 m, a range that includes all Swedish hydro-power stations. For a schematic description of the two types, see figure 1.1.2. The Kaplan turbine is characterized by the fact that not only the guide vanes, but also the turbine blades are adjustable and can therefore be matched to the current flow. However, the draft tube can not be adjusted. The efficiency of the draft tube is very important for a water turbine working at low head, and it is determined by how well the flow responds to the geometry. The design of many draft tubes in use today are

---

[1] James B Francis (1815-1892).

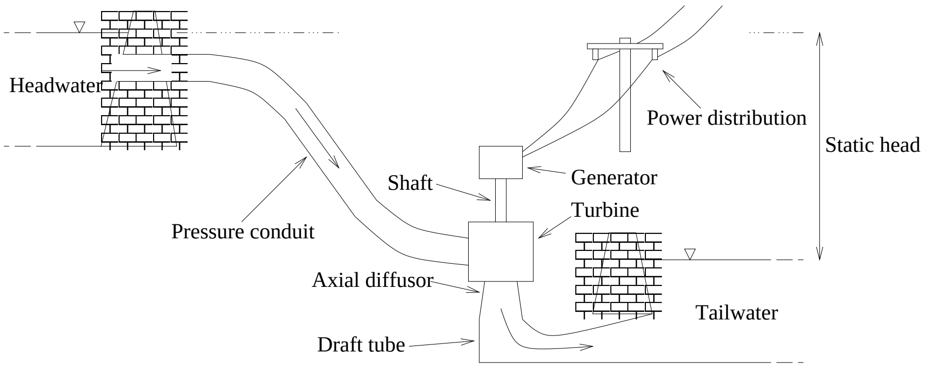
Headwater
Pressure conduit
Shaft
Generator
Turbine
Power distribution
Static head
Axial diffusor
Draft tube
Tailwater

FIGURE 1.1.1: Overview of a typical hydro-power plant including related glossary.

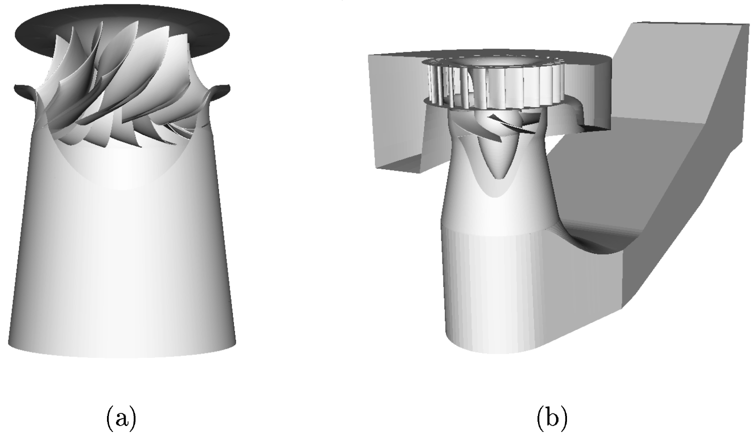
(a) (b)

FIGURE 1.1.2: (a) A Francis runner at the entrance of the axial diffuser; (b) The geometry of the Kaplan turbine of Hölleforsen, including the draft tube and the spiral casing. Also visible are the adjustable guide vanes just above the runner.

far from satisfactory, but when refurbishing old hydro-power plants there are possibilities to modify the draft tubes. A hydrodynamically improved design can increase the overall efficiency by 1.5% and yield a more reliable power plant. Usually only the runner and wicket gate are refurbished. However, the importance of adjusting the draft tube to the new flow conditions should not be underestimated. If this is disregarded, the stability of the flow and the efficiency may deteriorate.

Frequently the power plant has to run at non-optimal operating conditions (off-design). At off-design the water exits the runner with a strong vortical (swirling) flow. This vortical flow gives rise to a strong unsteady vortex core. In Francis turbines, the oscillations of the vortex can give rise to pressure fluctuations and vibrations of a magnitude that may dramatically decrease the efficiency, but may also cause structural damage to the turbine. The same kind of oscillations are present in Kaplan turbines as well, but of a lower amplitude. They will not cause structural damage but may have a serious impact on the efficiency. The Kaplan turbine draft tube are more sensitive to flow separation, which can be triggered by the pressure fluctuations. The customer demands warranties with respect to both efficiency and vibrations/noise. It is very important to be able to give warranties accurate enough for making reliable economical estimates of the investments.

1.2 The Draft Tube

The purpose of the draft tube of a water turbine is to reduce the exit velocity with a minimum loss of energy. Geometrically the draft tube is a fairly simple device; a bending pipe diverging in the streamwise direction, as in figure 1.1.2. However, the dynamical processes of the flow in a draft tube are very complex and many unsteady effects have been observed. The flow is dominated by large anisotropic turbulent motions, which effects the standard turbulence models fail to predict. Hence, there is a need to determine what features that are most crucial for a reliable numerical result. To accurately model this complex flow it is necessary to first examine the nature of the swirling flow in a similar but simpler geometry, like a straight conical diffuser. A diffuser is a duct of which the cross-sectional area increases in the streamwise direction, i.e. a diverging channel. Diffusers are used in many applications where a transfer of kinematic energy into (static) pressure energy is desired, including most kinds of turbo- and hydraulic machinery. In the design of a diffuser there are two major phenomena to take into account. Too rapid expansion (divergence of channel) can make the wall boundary layer separate, which leads to large losses. If the expansion is too slow the diffuser must be made longer and consequently the fluid will be exposed to an excessive area of walls. This will lead to larger wall friction losses and a more expensive construction. The optimal rate of expansion is obviously where the sum of these losses are minimized. Many times there are spatial restrictions of the size of the diffuser that also increases the importance of an optimal design.

1.3 Some Implications of Swirling Flow

A swirling flow is a flow rotating around an axis, most often an axis of geometrical symmetry. As already mentioned in section 1.1, the implications of swirling flow can be severe. But what is so special about swirling flow? Well, whenever a swirl component of the velocity vector is present, a radial pressure gradient is also found. This can, if the gradient is strong enough (i.e. for swirl numbers $S > 1$ [1]), give rise to recirculation and vortex breakdown, as well as formation of unsteady *vortex ropes*. A vortex rope is a coherent structure located in the center of the swirling flow, reminiscent of (guess what) a rope. It is the result of a symmetrical instability and is most often apparent in the shape of a cork-screw. Vortex breakdowns of swirling flow originates from internal stagnation points. They have been observed to wander back and forth along the streamwise axis with amplitudes depending on both the Reynolds number and the swirl intensity, see Faler et al. [4]. The same authors found recirculation zones that were dominated by low frequency velocity fluctuations with amplitudes exceeding the mean flow.

In practice, swirl can be generated in numerous ways. Guide vanes, tangential inlet velocity components, rotating honeycombs and propellers are frequently used. Every type of swirl generator creates a unique tangential velocity profile. While a rotating honeycomb may give a profile that resembles a solid body rotation, guide vanes and tangential inlets will give profiles with developed tangential boundary layers. Structures created at the inlet may persist for a long time depending of the type of generation, even though it has been shown that the mean flow decay more or less uniformly a few diameters length downstream [11]. Usually the tangential velocity profiles approximately assumes a combination of two characteristic vortex flows. In the center the tangential component resembles a forced vortex (solid body rotation) and elsewhere the tangential flow can be considered a free (irrotational) vortex. The combination described is often referred to as a *Rankine*[2] *vortex*, see figure 1.3. Mathematically the Rankine vortex can be described as

$$U_\theta(r) = \begin{cases} U_0 r/R, & r \in (0, R) \\ U_0 R/r, & r \in (R, \infty) \end{cases} \tag{1.3.1}$$

which is a crude estimation of a real vortex. It will nevertheless serve as a basis for understanding the flow field. The central region, the *forced vortex region* has radially constant vorticity. In the outer, *free vortex region*, the vorticity is zero. The concepts of vorticity and vortexes are not related.

---

[2] W J M Rankine (1820-1872), Scottish engineer.

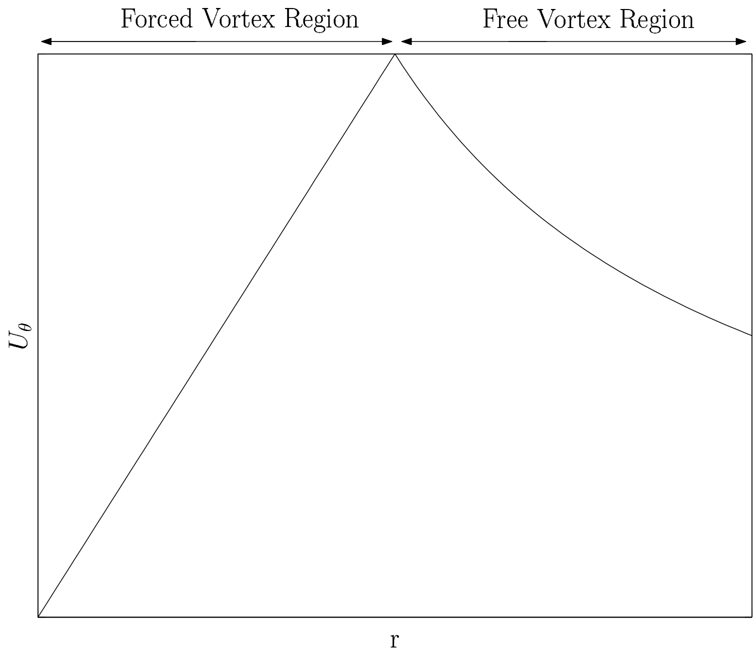

FIGURE 1.3.3: A Rankine vortex. It is a crude approximation of a tangential velocity profile of swirling pipe flow, but is used as a basis for understanding the rotating flow field. The free vortex region is an example of irrotational flow, while the forced vortex region resembles solid body rotation.

While a vortex is a coherent structure, vorticity is a vector describing the rotation of the flow field at a point.

1.4 Methods and Software

The equations governing fluid motion are the Navier-Stokes equations. The exact solution to these equations would provide an answer to most (if not all) matters concerning the flow. Due to issues discussed in appendix B, the exact solutions to the Navier-Stokes equations are not obtainable for real, industrial flow problems. Instead, some kind of averaged or filtered equations are solved. Even though the solutions to the averaged equations are not exact, they can still provide a detailed description of the mean features of the flow field. In this aspect CFD is outstanding. However, some caution must be taken when interpreting the solutions of the averaged equations.

For the calculations in this work the CALC-PMB CFD software has been used. CALC-PMB is developed at the Division of Thermo and Fluid Dynamics at Chalmers University of Technology, Göteborg. This in-house code is based on the finite volume method and the pressure-velocity coupling is solved using the SIMPLEC algorithm [3]. Conformal block structured boundary fitted coordinates are used and the code is parallelized for three-dimensional flows by domain decomposition. MPI is used for the exchange of information between the different processes/blocks, and two ghost cells are employed at the block interfaces to enable different first and second order discretization schemes. The principal unknowns are the Cartesian velocity vector components (U, V, W) and the pressure (P). To avoid spatial oscillations of the pressure field over the collocated (non-staggered) grid arrangement, Rhie & Chow interpolation is applied for convections through the cell faces. For the discretized (linearized) system of equations, TDMA is implemented as the standard algorithm. For further details, see [8].

The geometries and the grids are generated in the ICEM CFD/CAE commercial software. For post-processing, the Ensight commercial software has been employed.

1.5 The Experimental Data

The experimental data used for comparison in this work has been provided by Ole Gunnar Dahlhaug of NTNU, Trondheim, Norway. The measurements were a part of his Ph.D. thesis [1], in which all details of the experimental setup can be found. In short: The data were sampled by an LDA probe at three different locations, referred to as section A, B and C, see figure 3.2.1. The Reynolds number of the experiment, which from now will be referred to as Re_0, was 2,800,000. This number is based on the bulk velocity and the diameter of the pipe upstream of the diffuser inlet. Dahlhaug investigated several cases of swirling (conical) diffuser flow, including the flow through a diffuser followed by a bend, the flow through a bend followed by a diffuser and the flow through a diffuser without any bend. Dahlhaug also examined the behavior at several different swirl numbers ($S = \frac{1}{R}\frac{\int_A r u_{axial} u_{tan}\, dA}{\int_A u^2\, dA}$) rating from $S = 0$ to $S = 0.7$. In this work only one of the cases set up by Dahlhaug are numerically analyzed; the case without any bend at a swirl number $S = 0.35$.

Chapter 2

Governing Equations

The two gentlemen to whom the discovery of the equations governing fluid motion are ascribed are the French engineer/mathematician C L M H Navier (1785-1836) and the English mathematician G G Stokes (1819-1903). Even though almost 200 years have passed since the equations were first formulated, they are still subject to extensive research. In this section, the Navier-Stokes equations, and a few others, are introduced.

2.1 Equations of Motion

A flow can be considered incompressible if the density is constant in time and space. From the principle of mass conservation, the continuity equation for incompressible flow can be derived:

$$\partial_j u_j = 0 \tag{2.1.1}$$

The incompressible Navier-Stokes equations can be expressed as

$$D_0 u_i = -\frac{1}{\rho}\partial_i p + \nu\,\partial_j \partial_j u_i \tag{2.1.2}$$

where the operator

$$D_0 \equiv \partial_0 + u_j \partial_j \tag{2.1.3}$$

is the substantial (material) derivative.

2.2 The Averaged Equations - RANS

The governing equations are usually averaged. Depending on the underlying assumptions made when choosing which type of average to employ, the solution obtained from a calculation must be interpreted accordingly. These matters will be discussed thoroughly in appendix B. Anyhow, any averaging of non-linear equations will result in additional unknowns that must be modeled or related to the mean quantities through a constitutive relation. In the case of the Navier-Stokes equations the additional unknowns turn out to be correlations of fluctuating velocities. By introducing the ensemble average, $< x_i >= \lim_{N\to\infty} \frac{1}{N}\sum_{i=1}^{N} x_i$, there is a way to separate turbulence from the mean flow. The Reynolds[1] decomposition is defined as

$$u_i =< u_i > + u_i' = U_i + u_i' \tag{2.2.4}$$

and has a few nice properties. The ensemble average of a fluctuation is per definition equal to zero

$$< u' >\equiv 0 \tag{2.2.5}$$

and

$$<< u_i >>=< u_i > \tag{2.2.6}$$

These properties are extensively used in the derivation of all averaged equations below. In steady flow the ensemble average can be exchanged to a time average without loss of the properties of above. If the flow is unsteady a few other assumptions must be made, see appendix B. The basic equations for both applied CFD and theoretical research has been the *(U)RANS* equations, which are derived by inserting the Reynolds decomposition, equation (2.2.4), into equation (2.1.2). The unknown function U_i is the *mean* solution to the equations.

$$\partial_0 U_i + U_j \partial_j U_i = -\frac{1}{\rho}\partial_i P + \nu\, \partial_j \partial_j U_i - \partial_j < u_i' u_j' > \tag{2.2.7}$$

The last term in equation (2.2.7) is the gradient of the *Reynolds stress tensor*. It introduces six unknown quantities which must be modeled in order to close the system of equations. See next chapter for the closure model used in this work and appendix C for additional examples.

2.3 Reynolds Stress Equation

To close the system of equations of above, an equation for the Reynolds stress is needed. A transport equation for the Reynolds stresses can be derived from equations (2.1.2) and (2.2.7),

---

[1] Osbourne Reynolds, (1842-1912).

$$\begin{aligned}
&\partial_0 < u'_i u'_j > + U_k \partial_k < u'_i u'_j > = < \frac{p'}{\rho}(\partial_j u'_i + \partial_i u'_j) > - \\
&\quad < u'_j u'_k > \partial_k U_i - < u'_i u'_k > \partial_k U_j - \partial_k \left\{ \frac{1}{\rho} < p' u'_i > \delta_{kj} + \right. \\
&\quad \left. \frac{1}{\rho} < p' u'_j > \delta_{ki} + < u'_i u'_j u'_k > + 2\nu \left(< s'_{ik} u'_j > + < s'_{jk} u'_i > \right) \right\} + \\
&\quad 2\nu \left(< s'_{ik} \partial_k u'_j > + < s'_{jk} \partial_k u'_i > \right)
\end{aligned} \tag{2.3.8}$$

where $s'_{ij} = \frac{1}{2}\left(\partial_j u'_i + \partial_i u'_j\right)$. After some rearrangements and by renaming the Reynolds stress tensor $\tau_{ij} = - < u'_i u'_j >$

$$\begin{aligned}
\partial_0 \tau_{ij} + U_k \partial_k \tau_{ij} &= P_{ij} - \Pi_{ij} + \partial_k \left(\nu \partial_k \tau ij + C_{ijk} \right) + \varepsilon_{ij} \\
P_{ij} &= -\tau_{jk} \partial_k U_i - \tau_{ik} \partial_k U_j \\
\Pi_{ij} &= < \frac{p'}{\rho}(\partial_j u'_i + \partial_i u'_j) > \\
C_{ijk} &= \frac{1}{\rho} < p' u'_i > \delta_{kj} + \frac{1}{\rho} < p' u'_j > \delta_{ki} + < u'_i u'_j u'_k > \\
\varepsilon_{ij} &= 2\nu < \partial_k u'_i \partial_k u'_j >
\end{aligned} \tag{2.3.9}$$

The derivation of the Reynolds stress equation yields a large number of new unknowns, but can still serve as a foundation for the understanding of the Reynolds stress and the turbulent transport.

2.4 Turbulent Kinetic Energy Equation

By contracting the indices of equation (2.3.9) and dividing by two, an equation for the turbulent kinetic energy (per unit mass) k is obtained:

$$\begin{aligned}
&\partial_0 k + U_j \partial_j k = - < u_i u_j > \partial_j U_i + \\
&\quad \partial_j \left\{ \frac{1}{\rho} < p u_i > \delta_{ji} + \frac{1}{2} < q^2 u_j > + 2\nu < s_{ij} u_i > \right\} \\
&\quad -2\nu < s_{ij} s_{ij} >
\end{aligned} \tag{2.4.10}$$

This equation is often written in a condensed form:

$$\begin{aligned}
\partial_0 k + C_k &= P_k + D_k - \varepsilon \\
C_k &= U_j \partial_j k \\
P_k &= - < u_i u_j > \partial_j U_i \\
D_k &= -\partial_j \left\{ \frac{1}{\rho} < p u_i > \delta_{ji} + \frac{1}{2} < q^2 u_j > + 2\nu < s_{ij} u_i > \right\} \\
\varepsilon &= 2\nu < s_{ij} s_{ij} > \\
q^2 &= < u_i u_i > \\
k = \frac{1}{2} < u_{ii} > &= \frac{1}{2} < u_1^2 + u_2^2 + u_3^2 >
\end{aligned} \tag{2.4.11}$$

Above is the definition of the *real dissipation* ε; the amount of kinetic energy that is transfered to internal energy. Turbulence modelers often prefer a reorganized form of the diffusion and dissipation terms,

$$D_k = -\partial_j \left\{ \frac{1}{\rho} < p u_i > \delta_{ji} + \frac{1}{2} < q^2 u_j > + \nu \partial_j k \right\} \tag{2.4.12}$$

$$\varepsilon = \nu < \partial_j u_i \partial_j u_i > \tag{2.4.13}$$

where the sign of ε is always known. It is the latter definition that will be implied throughout this work. The two definitions of ε is identical if the turbulence is homogeneous, i.e. if the there is no (spatial) gradients of average quantities. Many flows are approximated as *locally homogeneous*[2]. The k-equation is often subject to analytic studies, so also in this work (see appendix A).

2.5 Filtered Equations and the LES

Another way of averaging is to *filter* the equations. A time filter can be defined as

$$\hat{u}_i(\mathbf{x},\mathbf{t}) = \frac{1}{T} \int_{t-T/2}^{t+T/2} u_i(\mathbf{x}, \tau)\, d\tau \tag{2.5.14}$$

and a spatial (3D) filter frequently used in LES can be expressed as

$$\hat{u}_i(\mathbf{x},\mathbf{t}) = \frac{1}{\Delta V} \int_{\Delta V} \tilde{u}_i(\mathbf{x}, t)\, dV \tag{2.5.15}$$

---

[2] Relations among derivative moments can be approximated as though they were homogeneous.

A filter have some special properties,

$$\widehat{\hat{(\cdot)}} \neq \hat{(\cdot)} \tag{2.5.16}$$

which means that (as opposed to averaging) a second filtering of a filtered variable yields a new unknown, and filtering a fluctuation

$$\hat{u'} \neq 0 \tag{2.5.17}$$

will not yield zero. By applying a filter to the unknown function and thereby solving for a smoother solution than the exact, the LES equations are obtained, i.e.

$$\partial_0 \hat{u}_i + \hat{u}_j \partial_j \hat{u}_i = -\frac{1}{\rho}\partial_i \hat{p} + \nu\, \partial_j \partial_j \hat{u}_i - \partial_j \tau_{ij}^{sgs} \tag{2.5.18}$$

where the subgrid stress tensor τ_{ij}^{sgs} is defined as

$$\tau_{ij}^{sgs} = \widehat{u_i u_j} - \hat{u}_i \hat{u}_j \tag{2.5.19}$$

The reader may observe that the only difference from the RANS equations is the form of the stress tensor. In this case it can also be defined as

$$\tau_{ij}^{sgs} = L_{ij} + C_{ij} + R_{ij} \tag{2.5.20}$$

where the terms

$$\begin{aligned} L_{ij} &= \widehat{\hat{u}_i \hat{u}_j} - \hat{u}_i \hat{u}_j \\ C_{ij} &= \widehat{\hat{u}_i u'_j} + \widehat{u'_i \hat{u}_j} \\ R_{ij} &= \hat{u}'_i \hat{u}'_j \end{aligned} \tag{2.5.21}$$

are called *Leonard Stress*, *Cross terms* and *Reynolds SGS stress* respectively.

Chapter 3

Numerical Procedure

This chapter concerns the numerical considerations. The setup of boundary conditions and the grid design are discussed. Six cases have been studied and the computations were done over three different grids and at two different Reynolds numbers. For a complete list of the cases referred to, see table 3.1. The (coupled) system of six non-linear partial differential equations were discretized by the *van Leer* second order scheme. The complete mathematical setup is the subject of the following section.

Case	*Grid*	*Re*	*Steady/Unsteady*
1:1	1	Re_0	Steady
1:2	1	Re_0	Unsteady
2:1	2	$\mathrm{Re}_0/10$	Steady
2:2	2	$\mathrm{Re}_0/10$	Unsteady
3:1	3	$\mathrm{Re}_0/10$	Steady
3:2	3	$\mathrm{Re}_0/10$	Unsteady

TABLE 3.1: Denotation of the different cases. $\mathrm{Re}_0=2.8 \cdot 10^6$.

3.1 The System of Equations

The equations that were solved are the (U)RANS equations and Wilcox (88) $k-\omega$ turbulence model:

$$\begin{aligned}
\partial_0 U_i + U_j \partial_j U_i &= -\frac{1}{\rho}\partial_i P + \nu\, \partial_j \partial_j U_i - \partial_j < u_i' u_j' > \\
\partial_i U_i &= 0 \\
- < u_i u_j > &= 2\nu_t S_{ij} - \frac{2}{3} k \delta_{ij} \\
\nu_t &= k/\omega \\
\partial_0 k + U_j \partial_j k &= P_k^{model} + \partial_j \left((\nu + \nu_t/\sigma_k) \partial_j k \right) - \varepsilon \\
\partial_0 \omega + U_j \partial_j \omega &= \partial_j \left((\nu + \nu_t/\sigma_\omega) \partial_j \omega \right) - \frac{\omega}{k} (c_{\omega 1} P_k^{model} + c_{\omega 2} k \omega) \\
P_k^{model} &= \nu_t \left(\partial_j U_i + \partial_i U_j \right) \partial_j U_i \\
\varepsilon &= \beta \omega k
\end{aligned} \tag{3.1.1}$$

where the closure coefficients are

$$\beta = 0.09,\ c_{\omega 1} = 5/9,\ c_{\omega 2} = 3/40,\ \sigma_k = \sigma_\omega = 2 \tag{3.1.2}$$

The $k-\omega$ turbulence model was chosen due to its good reputation and its robustness.

3.2 The Computational Domain

The diffuser used in the experiment has an inlet radius of 50 mm and an outlet radius of 75 mm. This gives an area ratio, $A_R = 2.25$. To have something close to a fully developed swirling channel flow at the inlet, the swirl generator was in the experiment located 2.71 m upstream of the diffuser inlet. For the calculations, the pipe is cut 130 mm upstream of section B, and 355 mm downstream of section C, see figure 3.2.1. Velocity profiles from different computational cases has been analyzed at sections B, C, D, E and F.

3.3 Boundary Conditions

The inlet boundary conditions for the mean velocities were linearly interpolated from the measured data of section B provided by Dahlhaug [1]. Due to the lack of measured data of k in the free vortex and near wall region at section B, standard boundary conditions for non-swirling pipe flow were

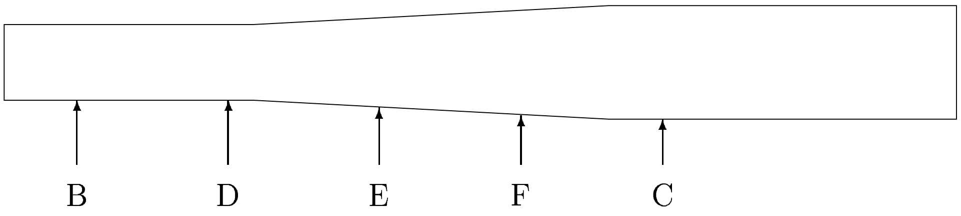

FIGURE 3.2.1: The computational domain of the conical diffuser and the sections referred to. Experimental values are supplied at sections B and C. Sections D to F describe the additional locations of choice for comparison of the different computational cases. Section A is located upstream of the computational domain, and is thus not present in the figure.

used for the turbulent quantities. To evaluate the effect of these boundary conditions on the mean flow, the inlet were in the calculations moved 130 mm upstream of section B. According to Dahlhaug, the tangential and axial velocity components do not change significantly upstream of section B, and the measured data of section B may therefore be used as boundary conditions at this cross-section. The standard boundary conditions for the turbulent quantities demands an approximation of a fully developed pipe flow velocity profile. This can be obtained by [15]

$$V = U_{cl} \left(\frac{R - r}{R} \right)^{1/7} \tag{3.3.3}$$

where the centerline velocity U_{cl} was chosen to get the right mass flow through the domain. The gradient of this profile was used for calculating the inlet boundary conditions of k and ω, see equation (3.3.4).

$$\begin{aligned} U_i &= U_i^{exp} \\ k &= C_\mu^{-1/2} l_m^2 \left(\partial_r U_{axial} \right)^2 \\ \omega &= \frac{k^{1/2}}{C_\mu^{1/4} l_m^2} \end{aligned} \tag{3.3.4}$$

where

$$\begin{aligned} C_\mu &= 0.09 \\ l_m &= min(\kappa y,\, \lambda \delta) \\ \kappa &= 0.41 \\ \lambda &= 0.13 \\ \delta &= R \end{aligned} \tag{3.3.5}$$

The common kinematic (non-porous walls) and viscous (no slip) conditions were used at the walls. The wall boundary conditions can be summarized as

$$\begin{aligned} U_i &= \mathbf{0} \\ k &= 0 \\ \omega &= \frac{6\nu}{C_{\omega 2} y^2} \end{aligned} \tag{3.3.6}$$

Convective or Neumann boundary conditions were used at the outlet:

$$\begin{aligned} \partial_0 U_i + U_b \partial_n U_i &= \mathbf{0} \\ \partial_n k &= 0 \\ \partial_n \omega &= 0 \end{aligned} \tag{3.3.7}$$

The convective boundary condition resembles the Neumann boundary condition if the flow is steady.

3.4 The Grids

The geometry and the grids were constructed using the ICEM CFD software. The axisymmetric geometry was captured by an O-grid formation, where a block centered along the geometrical axis is surrounded by four wall-bounded blocks, see figure 3.4.2. Coarse grids designed for wall functions were used in cases 1:1-2:2. This means that the first interior nodes should be placed in the log-layer[1] at $y^+ \in (30, 100)$. A posteriori verification of this criteria were done by analyzing the distributions of the first interior wall nodes over y^+ values. These are shown in figure 3.4.2. When using LRN[2] models (no wall or damping functions), a much finer grid was used. In this case the first node was placed at a wall distance corresponding to $y^+ < 5$. In the wall normal direction the grids in the wall bounded blocks were stretched by a factor 1.1 (case 2:1-3:2) or 1.2 (case 1:1-1:2). The total number of cells were 100,000 for grids 1-2, and the grids were divided into ten blocks for parallel computing. The size of grid 3 was 781,250 cells and a similar domain decomposition was applied. The computations were considered converged when all normalized residuals were of the order of 10^{-6}. The residuals of the momentum equations were normalized with the corresponding convection and the pressure (continuity equation) with the mass flow rate.

---

[1] Even though it may not exist any log-layer for this type of flow, it is only one among many other approximations.

[2] LRN is an abbreviation of 'low Reynolds number' and refer to the *local* Reynolds number $Re_{local} = \frac{u^* n}{\nu}$ where u^* is the friction velocity ($u^* = \sqrt{\tau_w/\rho}$), n is the wall normal distance and τ_w is the wall shear stress.

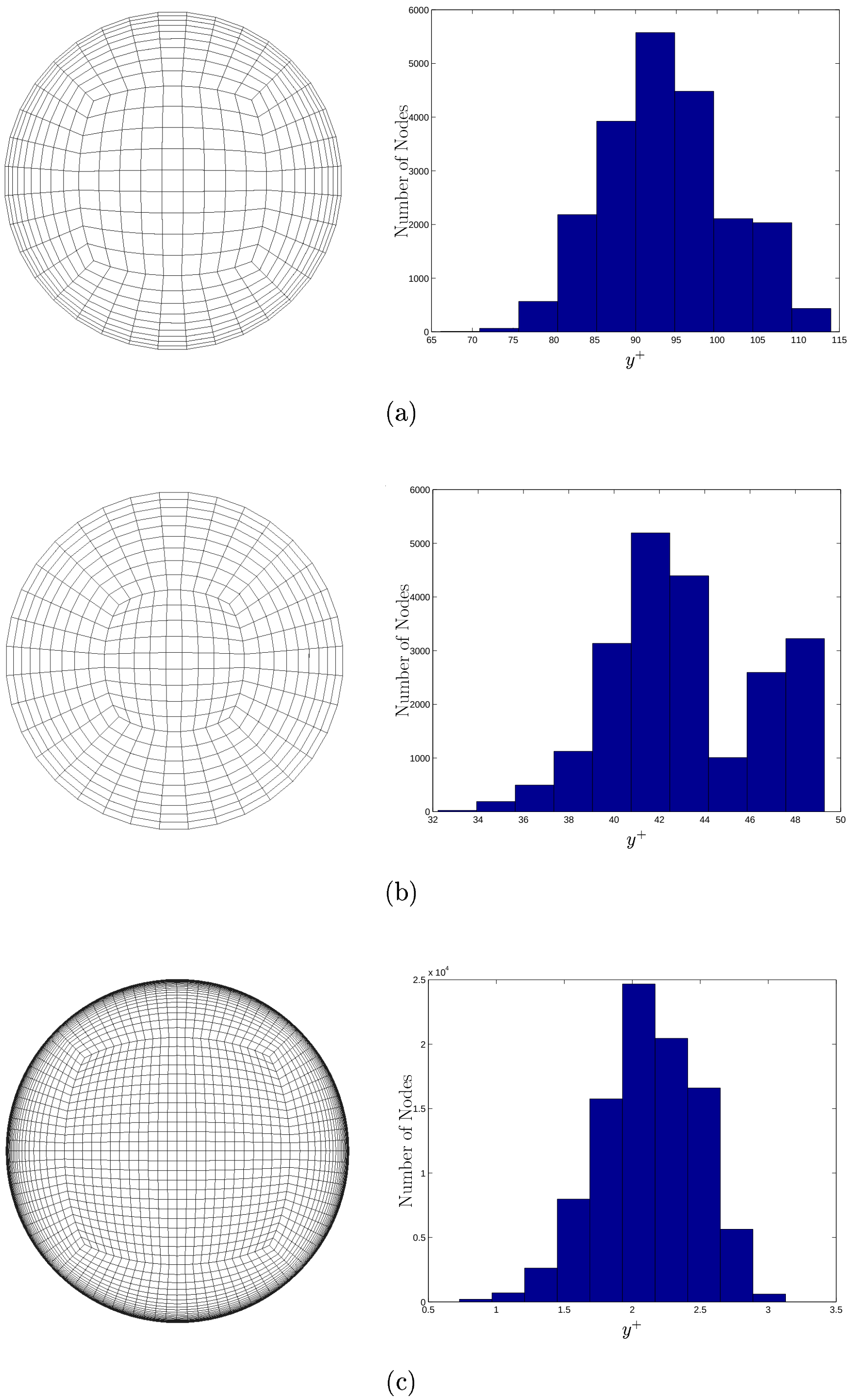

FIGURE 3.4.2: The grids and the corresponding distribution of first interior nodes over y^+ values. (a) Grid 1 has 100,000 nodes and has a stretch factor of 1.2 in the wall normal direction; (b) Grid 2 has 100,000 nodes and a stretch factor of 1.1 is employed; (c) Grid 3 is the largest grid. It has 781,250 nodes and the stretch factor is 1.1. The stretch is only applied in the wall-bounded blocks.

Chapter 4

Results and Discussion

In this chapter the results from the (U)RANS computations are evaluated. The unsteady computations converged to the same solution as their steady counterparts due to issues discussed in section 4.5.1 and appendix C.4. Since they did not yield any additional information, they are not referred to in this section. To give an adequate description of the flow, visualizations of iso-surfaces, streamlines, smearlines and profiles of mean quantities are presented. The latter are compared to the experimental data. All 3D visualizations are made from data obtained from case 3:1, due to the good quality of the resolution. However, all large scale features were common to all cases. Figure 4.0.1 gives a qualitative picture of the flow field. The solutions to the equations were found to be asymmetric and in section 4.5 the origin and the physics behind the symmetry breaking are discussed.

4.1 Vortex Structures and Boundary Layer Interaction

By examining the iso-surfaces of normalized helicity, i.e. the projection of the normalized vorticity vector on the normalized velocity vector ($\varphi = \frac{\omega_i u_i}{|\omega_i||u_i|}$), the largest values to the magnitude are naturally found in the central vortex; the swirl itself, see figure 4.1.2 (a). Due to the alignment of the mean flow and the negative y-axis, the sign of helicity will be negative for a counter-clockwise rotation of the flow field. Positive helicity are found in two particular spots just at the diffuser exit, see figure 4.1.2 (b), where the vorticity in the streamline direction changes sign. The feature is, as will be shown in the following section, strongly connected to the pressure asymmetry. The reversed vorticity is a necessary condition for the asymmetry of the central vortex. The topology of the counter-rotating vortices has some similarities

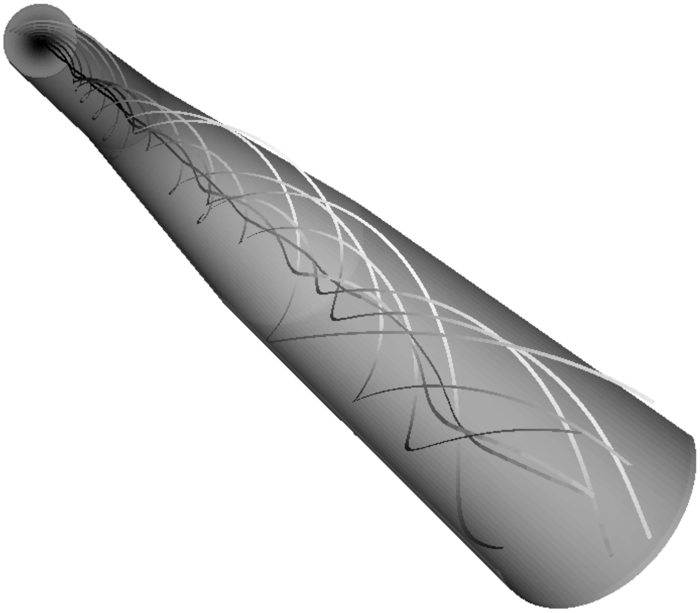

FIGURE 4.0.1: Streamlines and inlet pressure distribution where dark color represents low pressure. Particles are released along a radial line at a fixed tangential position at the inlet and are traced along the steady flow.

to the Taylor[1] vortices found in Couette[2] flow. The coherent structure of a Taylor vortex is distinct even if the flow is turbulent. As can be seen from figures 4.1.3 and 4.1.4, the complexity of the boundary layer is evident. Secondary (if not tertiary) flow is present from the entrance of the expansion and further down. The flow resembles features observed experimentally by, among others, Spohn et al. [14] and numerically by Sotiropoulos and Ventikos [13], see figure 4.5.9 and discussion in section 4.5. There is a strong coupling of the boundary layer to the counter-rotating vortices of the internal flow. At the diverging smearlines a positive radial velocity and consequently a thinner boundary layer will be found. The wall shear will be greater due to a higher velocity gradient, which is shown in figure 4.1.4 (a). The opposite situation is found at the converging streamlines. When wall functions were used, the asymmetry of the smearlines are also present but less evident.

---

[1] G I Taylor (1886-1975), British scientist.

[2] M F A Couette (1858-1943), French scientist.

4.2 The Pressure Distribution

The interaction of the diffuser and the swirling flow gives rise to several other interesting features, such as an asymmetric pressure distribution. As can be seen in figure 4.1.3 (b) the angle of thread of the iso-pressure surface is corresponding to the local flow direction. A look at the mean pressure profiles gives information about the pressure evolution; as the pressure rises through the diffuser there is a strong decay of the radial gradient, see figure 4.2.5. During the expansion, the discrepancy between the cases is obvious. The calculations over coarse grids are probably suffering from severe numerical diffusion, smoothing the radial pressure gradient. The pressure rise coefficients are compared in table 4.1. The two cases most suitable for comparison are cases 2:1 and 3:1, due to their common Reynolds number. The difference is about 2.6%. Case 1:2 is present in the table only to show the negligible difference between the steady and unsteady calculations, the values are identical to the forth decimal.

Case	*Re*	C_p
1:1	Re_0	0.5937
1:2	Re_0	0.5934
2:1	$\mathrm{Re}_0/10$	0.5737
3:1	$\mathrm{Re}_0/10$	0.5892

TABLE 4.1: Pressure rise coefficients, $C_p = \frac{P_{wall,C} - P_{wall,B}}{\frac{1}{2}\rho U_b^2}$. The wall pressure is averaged tangentially. $\mathrm{Re}_0 = 2.8 \cdot 10^6$.

4.3 The Mean Velocity Profiles

The mean velocity profiles is compared to experimental data in figure 4.3.6. In figure 4.3.6 (a), the locations of the sample stations is clear, but it is first after rescaling the picture the deviations are visible. A comparison of the computed and the measured data at section B reveals the quality of the inlet boundary conditions. There are some similarities to the idealized Rankine vortex described in chapter 1. In the center the radial gradients are almost constant (forced vortex region) and there are also inflection points ($\partial_r \partial_r U_\theta > 0$) like in the free vortex region of figure 1.3.

What is striking in figure 4.3.6 (b) is the discrepancy of the different cases during the expansion, especially for the tangential component. The discrepancy is an indicator of the complexity of the flow through the diffuser and is less obvious at the outlet. At section C, the measured axial velocity profile is not well represented by any computation. The total deviation (i.e. $\frac{1}{N}\sum_{n=1}^{N}\frac{U_{calc,n}-U_{exp,n}}{U_b}$) from experimental data is of the same order for the three calculations; 0.0461, 0.0890 and 0.0750 for cases 1:1, 2:1 and 3:1 respectively.

The discrepancies between the computed and measured data of axial velocities in the forced vortex region can to a large extent be explained by the choice of turbulence model, i.e. the Boussinesq assumption. Due to issues discussed in appendix A, the radial turbulent mixing will in this region be suppressed. The model however, will predict an isotropic turbulent viscosity and consequently over-estimate the radial turbulent mixing. Only second derivatives (i e $\partial_r\partial_r U_i$) of the velocity profiles will be affected by the error induced by the model. Since the tangential profile in the central region closely resembles a forced vortex and is an odd function of the radius, the radial second derivative will vanish. Hence, the tangential velocity profile will not suffer from the over-estimation of turbulent mixing.

The calculated magnitudes of deviation of above should not be considered estimates of the computational error. Even though case 1:1 gives the lowest deviation from experimental data, it is probably due to the wrong reasons. The difference in shape of the profiles of case 2:1 and 3:1 is a sign of strong grid dependence. Considering the higher *Re* in case 1:1, grid 1 must be regarded much more coarse than grid 2. As can be seen from figure 4.3.6, the local axial velocity maximum of the well resolved case 3:1 is closer to the centerline than the maximum of the not so well resolved case 2:1. From this, there are reason to believe that it is the grid resolution that determines the location of the local maximum. The least resolved calculation therefore gives the ‘best’ results, since the skewness of this profile best captures the skewness of the experimental data. If the reasoning of above is consistent, it is an example of where numerical errors can reduce errors induced by the turbulence model. All turbulence models depends on fully resolved mean gradients, but also the errors induced by unphysical behavior of the model will become more obvious if the gradients really are resolved.

4.4 The Turbulent Quantities

The plots of the evolution of turbulent kinetic energy in figure 4.4.7 shows how the turbulence gets smeared out during the expansion. There is a decay of turbulent kinetic energy in the axial direction. Evaluating the downstream behavior of the modeled turbulence, there seems to be a dependence of Reynolds number. Case 1:1, computed at $Re = Re_0$, display a decay of k much faster than the others. It turns out that the integral

$$P_k^{net} = \frac{2\pi}{U_0^2}\left(\frac{1}{A_{inlet}}\int_0^{R_{inlet}} k(r)r\,dr - \frac{1}{A_{outlet}}\int_0^{R_{outlet}} k(r)r\,dr\right) \tag{4.4.1}$$

is negative for both Reynolds numbers, but the magnitude is four times larger in case 1:1. Experimental data by Dahlhaug [1] confirms the calculated decrease of turbulent kinetic energy, see also appendix A.2 for a theoretical explanation of this behavior. In figure 4.4.7 (b) the axial and tangential normal stresses for the three cross-sections are plotted and the anisotropy of the turbulence is obvious. The high values of normal axial and tangential fluctuations at the center are due to the strong streamline curvature of this region. There is also a tendency of the downstream distribution of the calculated turbulent kinetic energy to move towards the center of the pipe. It may be regarded as an indication of erroneous inlet boundary conditions for the turbulent kinetic energy.

4.5 Instability of the Symmetric Mode

The predominant feature of the visualizations in section 4.1 is the asymmetry. The conical diffuser is axisymmetric, and the use of axisymmetric boundary conditions would suggest that the solution also is axisymmetric. However, even though solutions to the axisymmetric (two-dimensional) equation do exist, they will probably never be obtained in a real flow due to the instable properties of the three-dimensional equations/physics.

Experimental investigations by Spohn et al [14] as well as numerical by Sotiropoulos and Ventikos [13], concerning the three-dimensional structures of a confined swirling flow generated by a rotating disc (see figure 4.5.8) both show identical (steady) asymmetric behavior.

Though it may seem far-fetched to compare a swirling flow through a diffuser to a confined, recirculating flow in a cylindrical container with a rotating bottom, there are actually many similarities. Due to centrifugal forces, the near-bottom fluid is accelerated towards the walls of the cylinder. At the walls, the fluid is forced into an upwards motion, and a Stewartson[3] boundary layer is formed, see figure 4.5.8. The boundary layers in figures 4.5.9 (a) and (b) has converging/diverging streamlines, ordered in a near periodic manner. The periodicity of the computed smearlines in figure 4.1.4 is not as obvious, but a look at the velocity magnitude gradient ($\partial_r|U_i|$) reveals a clear periodicity of the boundary layer thickness. As the boundary layer thickness of the confined flow grows in the streamwise direction (figure 4.5.8), the effect of the boundary layer on the downward axial velocity component at the center of the cylinder is the same as in a diverging tube. The presence of an adverse pressure gradient is also common to both cases. Sotiropoulos and Ventikos suggests that the asymmetry observed in confined container flow is the result of outer disturbances from small but finite imperfections of a non-ideal environment. Outer disturbances will from now on be referred to as *forced* symmetry breaking. In the laboratory-environment, the forced symmetry breaking may be caused by noise/vibrations, thermal gradients or small asymmetries at the boundaries etc. It is almost impossible to exclude this randomness from reality, although Spohn et al. made sure that the disturbances did not emerge from imperfections at the walls. Numerically the disturbances are of a different nature. The numerical noise is hopefully not crucial in determining the path along which a solution converges. Instead, the disturbances arise from round-off errors of the coordinates of the nodes, asymmetries in the grid structure, CAD geometry or boundary conditions or even from the block topology of a multi-block computation. In the numerical case, it may be possible to isolate the source. However, whatever the source to a disturbance may be, the same solution seems to be obtained regardless of the origin of the (forced) symmetry-breaking phenomena. Further, since the non-symmetric solution obviously is more stable, it is far more interesting than the solution to an ideal problem. For sure, a real industrial flow will almost always be subject to some level of distortion.

---

[3] K Stewartson (1925-1983), English fluid dynamicist.

4.5.1 Spontaneous and Forced Symmetry Breaking

In an experiment similar to the one already mentioned, Hirsa et al. [5] examined the symmetry breaking disturbances in confined swirling flow with a free surface (instead of the top lid) using PIV. They made a clear distinction between forced and *spontaneous* symmetry breaking, and they found that a misalignment of the rotating floor and the cylinder axis in the order of 0.002 diameters was enough to create a asymmetric behavior different from the behavior of the fluid obtained after a spontaneous symmetry breaking. According to the authors, the spontaneous symmetry breaking is a Hopf bifurcation[4] resulting from an azimuthal instability of the bottom shear layer. The instability is produced by the turning of the boundary layer into the interior. The spontaneous symmetry breaking gave rise to a rotating wave at the free surface, and consequently a time-periodic pressure distribution in the container (which can correspond to the unsteady rotating vortex rope that has been found experimentally in draft tubes). The wave did not appear if a forced symmetry breaking disturbance was present. If a similar instability was to be found in the conical diffuser, it would not be addressed to a boundary layer. Instead, it would be triggered by the gradient of tangential velocity in the axial direction, which is quite evident (see figure 4.3.6) during the expansion. The decay of tangential velocity will create a similar turning, or tangential shear, of the fluid and if this instability is of decisive importance in this work, the source of outer disturbances may be important: If the spontaneous symmetry breaking gave rise to periodic pressure fluctuations they could have been found in the unsteady computations, if not destroyed by forced symmetry breaking features. This may very well be the case.

---

[4] H Hopf (1894-1971), Swiss mathematician. A Hopf bifurcation is a periodic mode originating from a state of symmetric time-invariant instability.

The phenomena of a rotating asymmetric pressure field has been found computationally by Ruprecht et al. [10], who investigated turbulence modeling of a swirling flow in a diffuser, very similar to the flow discussed in this work. Depending on the chosen turbulence model, they found steady symmetric solutions (which may be the time averaged solutions, see appendix B) or unsteady rotating asymmetric solutions. To summarize the notes of above: If there are no forced disturbances present, the solution may be unsteady. If a forced disturbance is imposed, it may 'lock' the flow in an asymmetric mode.

4.5.2 A Search for the Disturbance

All computational cases in this work show the same asymmetry, where the pressure iso-surface tends to lean towards the negative x-direction at the outlet. Hence, there must be a common source of distortion that triggers the instability of the symmetric mode. To derive the source of disturbance, four additional cases were set up:

I A reference case.

II Permutation of indices of the nodes.

III The grid rotated 45° around the streamwise (symmetry) axis.

IV As III, but the grid is also re-projected on the CAD geometry.

Permutation of indices affects the TDMA solver. The sweep direction of the solver may cause different rates of convergence in different parts of the block. This did however not affect the solution. If the grid topology were decisive to the asymmetry, the last two cases would yield a rotated solution. If small imperfections in the CAD-geometry was to be the possible source of disturbances, the rotated and projected case (case IV) would give the same solution as the reference, but the case where only the grid is rotated (case III) would yield a solution rotated by 45° degrees. This turned out to be the case, and figure 4.5.10 shows that the solution is determined by the CAD geometry. Analyzing the radius obtained from the CAD software when rotating the profile of the diffuser around an axis of (expected) symmetry, figure 4.5.11 was obtained. As can be concluded from the figure, the diffuser is neither circular or elliptic, but resembles a buckled shape. The symmetry error $(\frac{R_{max}-R_{min}}{R})$ is 0.92%. This is probably what triggers the symmetric instability. Also, it will seriously affect the inlet boundary condition for k which includes the square of the radial velocity gradient, see fig 4.5.10. The inlet boundary conditions for the velocities showed to be less sensitive to the geometry.

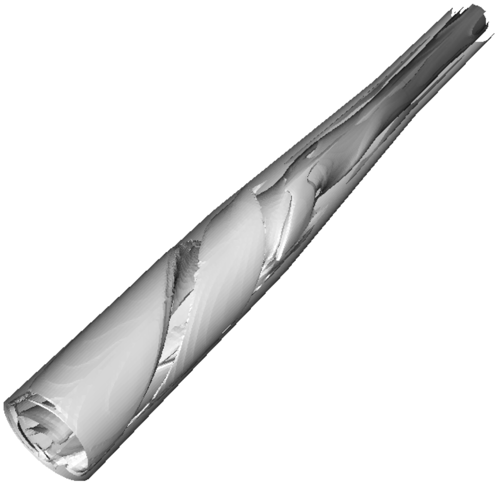

(a)

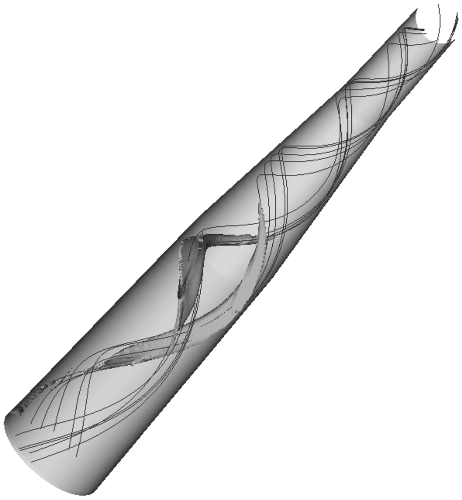

(b)

FIGURE 4.1.2: (a) Iso-surface of normalized negative helicity at a level of about -0.8; (b) Iso-surfaces of normalized positive helicity at a level of about 0.2, with streamlines emerging from the surface. The positive iso-surfaces fits perfectly inside the two valleys of the negative iso-surface. The twisting of the bunch of streamlines correlates to the change of sign of vorticity.

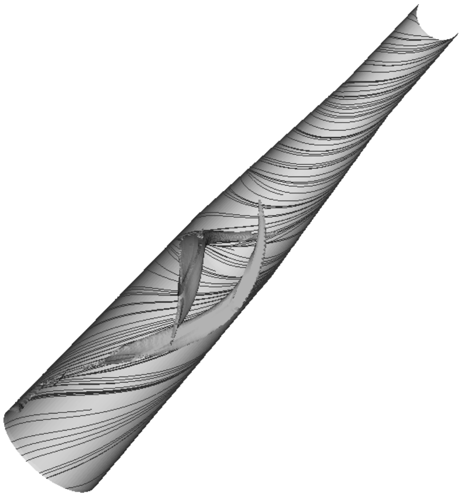

(a)

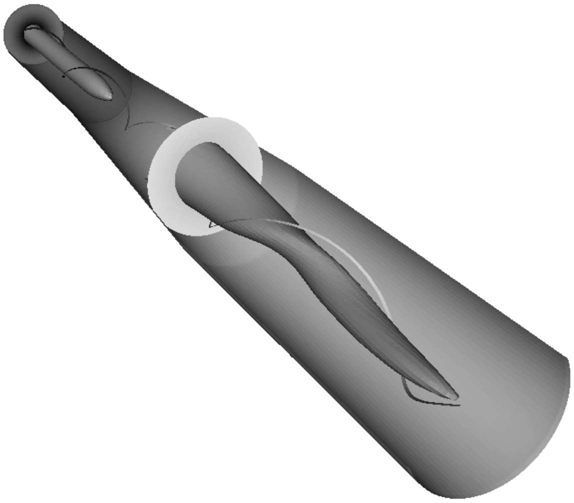

(b)

FIGURE 4.1.3: (a) Iso-surface of positive normalized helicity and the boundary layer interaction of the vortices, visualized by smearlines at the wall. (b) Two different iso-pressure surfaces and one streamline, along with planes of pressure distribution where dark grey denotes low pressure. The flow seems to follow the thread of the iso-pressure surface. The pressure rise is obvious from the cross-sectional planes.

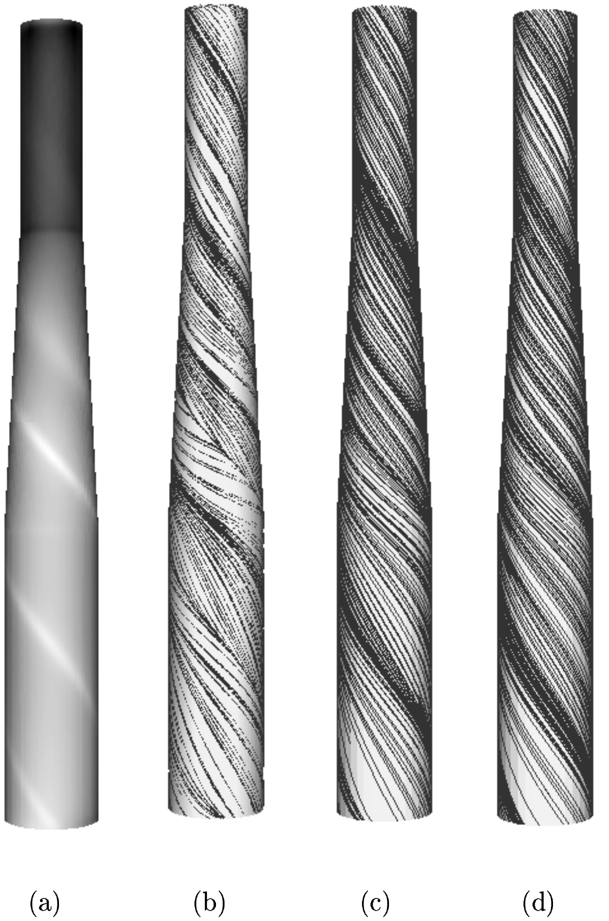

FIGURE 4.1.4: (a) Wall normal velocity magnitude gradient for case 3:1, where dark color equals high value. The light regions reveal a clear periodicity of the boundary layer thickness. (b) - (d) Smearlines for cases 3:1, 2:1 and 1:1 respectively. The use of wall functions in case 1:1 and 2:1 (fig (c)-(d)) makes the irregular structures less evident.

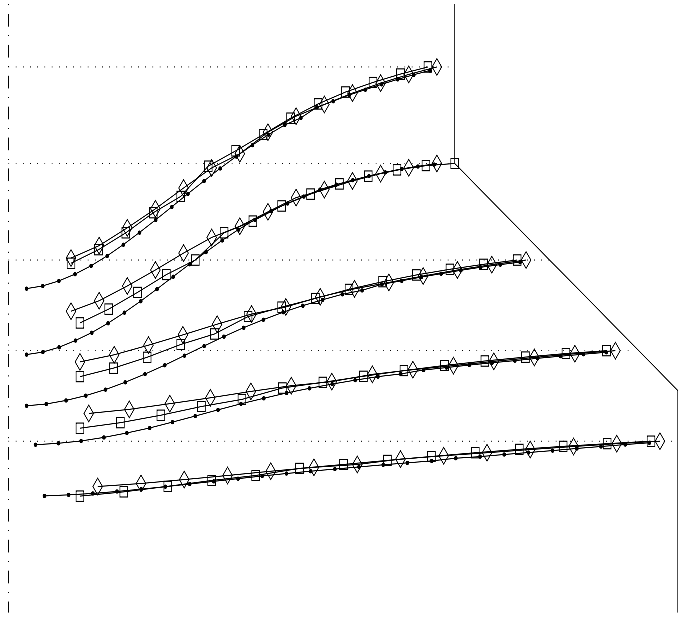

Figure 4.2.5: Pressure distribution profiles. In the figure, the profiles are fixed to zero at the wall in order to make the comparison more convenient. There is a correlation between grid resolution and and the relative value of the minimum. Markers: •: Case 3:1; □: Case 2:1; ◇: Case 1:1.

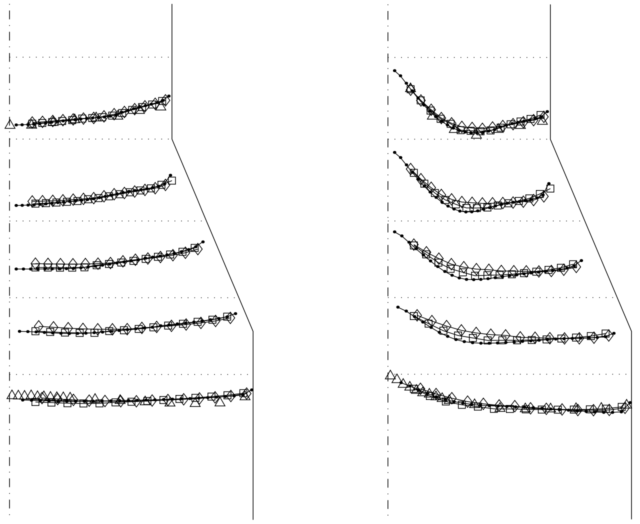

(a)

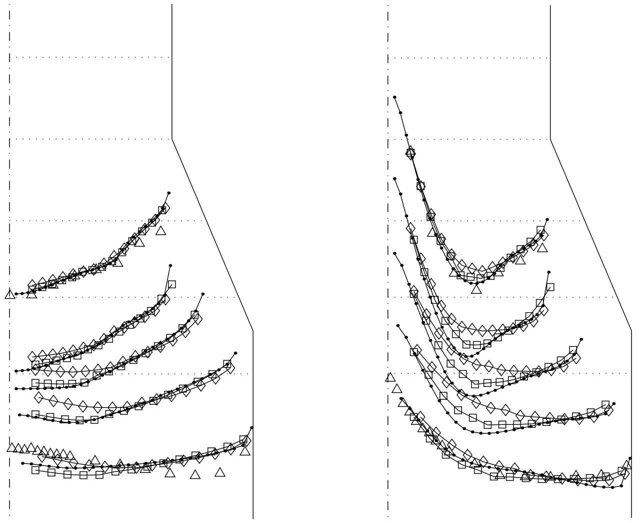

(b)

FIGURE 4.3.6: (a) Axial (left) and tangential velocity profiles. Markers: •: Case 3:1; □: Case 2:1; ◇: Case 1:1; △: Experimental data. All computed values are tangentially averaged. In figures (b) the data is re-scaled to expose the differences. The discrepancies among the cases are quite large during the expansion. The measured axial velocity component is not well represented by any computation but the computed tangential components are more consistent. The calculated values of case 1:1 are in best agreement with experimental data, but probably due to the wrong reasons, see section 4.3.

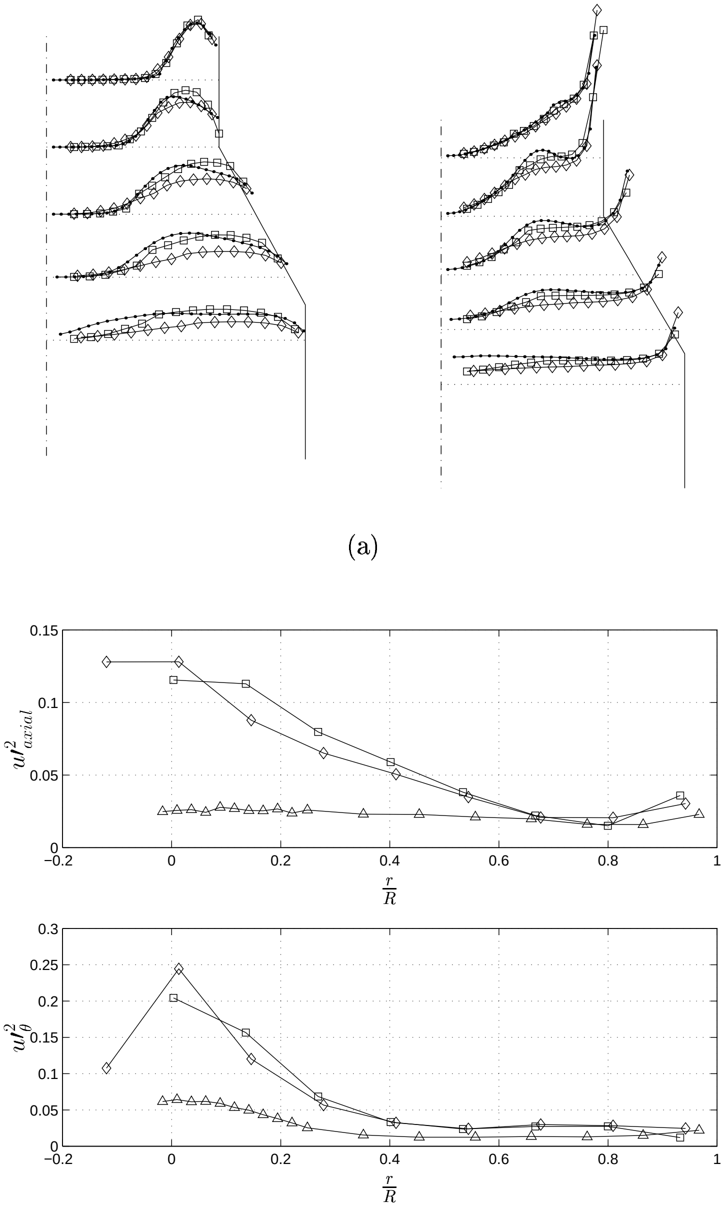

(a)

(b)

FIGURE 4.4.7: (a) Computed turbulent kinetic energy (left) and specific dissipation profiles. Markers: ●: Case 3:1; □: Case 2:1; ◇: Case 1:1. (b) Experimental data. Axial normal stresses (top figure) and tangential normal stresses (bottom figure). The normalized values are plotted over three different cross-sections. Markers: ◇: Section A; □: Section B; △: Section C. The decay of turbulent kinetic energy during the expansion is evident and can also be analytically deduced, see appendix A.2.

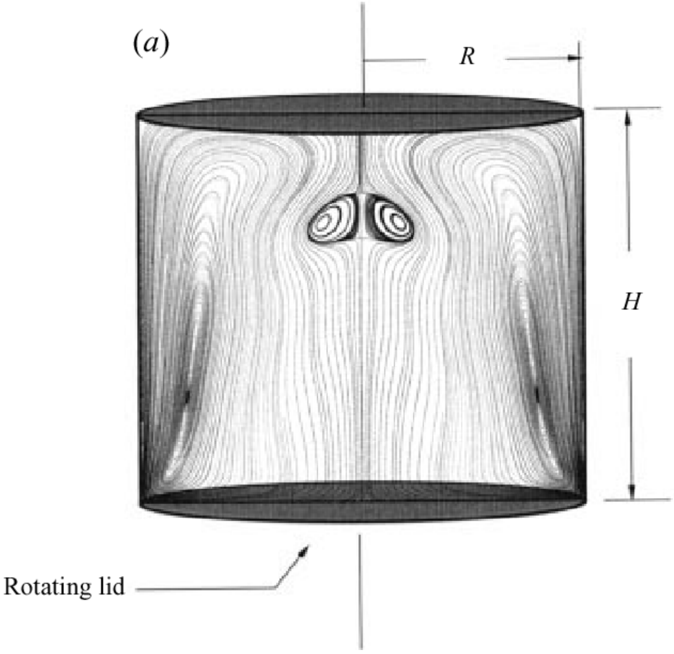

FIGURE 4.5.8: Calculated streamlines over a vertical cross-section in a confined swirling flow with a rotating bottom. The calculations were made by Sotiropoulos and Ventikos [13]. In the central region, the flow is moving axially downwards, and along the walls there is an upwards motion. As the wall boundary layer grows, the central flow will feel like it was subject to a geometrical expansion. Reprinted with permission from F. Sotiropoulos.

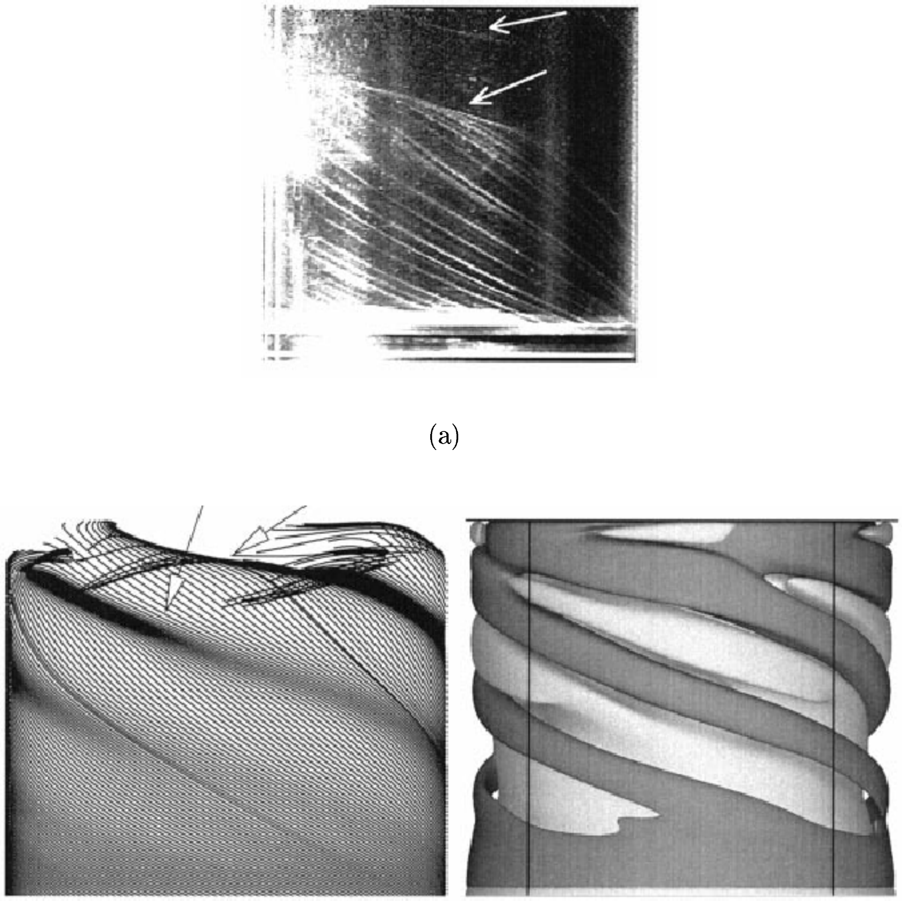

(a)

(b)

FIGURE 4.5.9: Smearlines and radial velocity iso-surfaces in a confined swirling flow with a rotating bottom. (a) Experimentally visualized smearlines by Spohn et al. (b) Smearlines (left) and iso-surfaces of radial velocity (right) computed by Sotiropoulos and Ventikos. As the wall boundary layer grow in the upwards direction, converging/diverging smearlines develop, a feature that also is found in the diffuser flow. Reprinted with permission from F. Sotiropoulos.

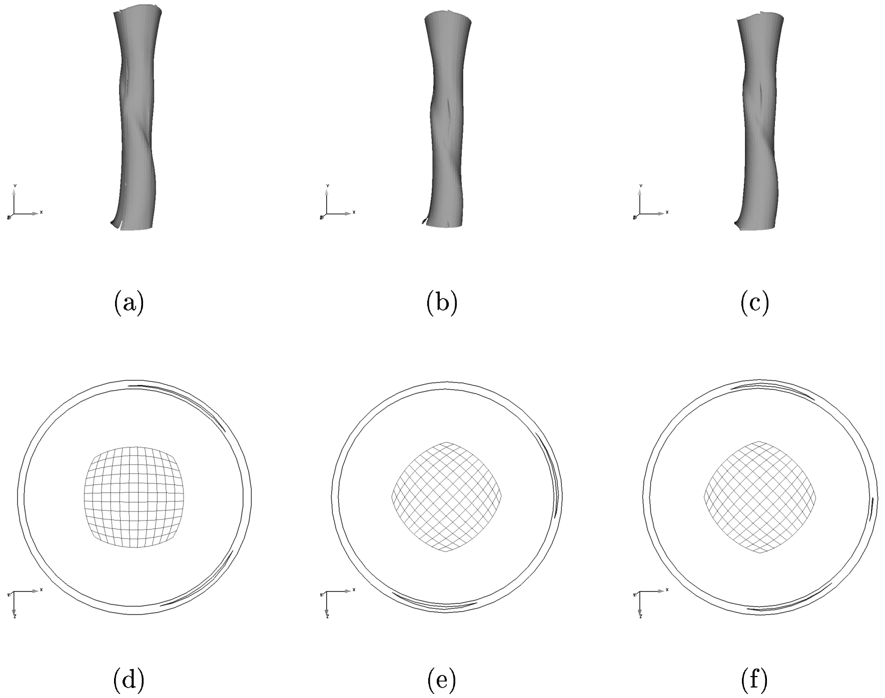

(a) (b) (c)

(d) (e) (f)

FIGURE 4.5.10: (a)-(c): Iso-surfaces of pressure. (a) Reference case. (b) The mesh rotated by 45°. (c) The mesh rotated and re-projected at the CAD geometry. It is obviously the CAD geometry that is crucial to the orientation of the asymmetry. (d)-(f): Iso-curves of inlet turbulent kinetic energy. Also shown is a block of the computational grid to clarify the orientation. (d): Reference case. (e): The mesh rotated by 45°. (f): The mesh rotated and re-projected at the CAD geometry.

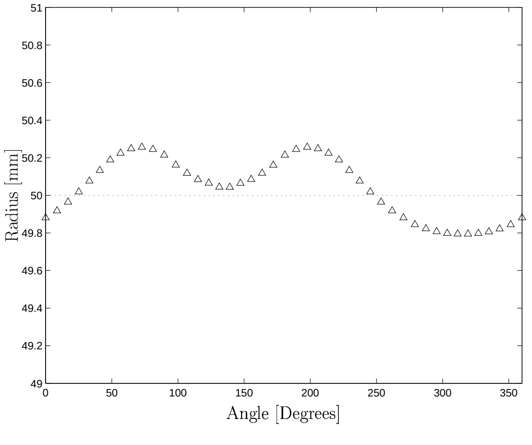

FIGURE 4.5.11: The radius of the diffuser inlet over the angle.

Chapter 5

Conclusions

The swirling flow in a conical diffuser is very complex and the converging/diverging smearlines along the walls reveal a high level of secondary flow during the expansion. Counter-rotating vortex structures are found at the diffuser exit. The asymmetric behavior is due to instabilities of the axisymmetric mode, and the disturbance that triggers the instability is imperfections in the CAD-geometry.

Similarities to confined swirling flow have provided a deeper understanding of the many phenomenas found in swirling diffuser flow.

The discrepancies regarding the agreements with experimental data are partly reminiscent from the nature of the turbulence model which overestimates radial turbulent mixing in the forced vortex region. There are experimental and theoretical evidence of a high level of anisotropy in swirling flow, which cannot be accurately predicted with the standard $k - \omega$ model that was chosen for the simulations.

The URANS computations did not yield any unsteady effects. This can also be explained by the choice of turbulence model, but another possible explanation is that the forced symmetry breaking disturbance, that is imposed by the geometry, may lock the flow in a steady asymmetric mode.

Chapter 6

Future Work

Further investigations of swirling flow in diffusers are needed. Different swirl numbers must be considered and also the influence of a bending geometry, which would to higher extent resemble the shape of a draft tube. To examine the anisotropic properties of the large scale turbulent motions, these must be computationally resolved using LES. This will give detailed information of unsteady behavior not obtainable by (U)RANS modeling. Especially the behavior of the central vortex rope are interesting. There are other advantages to LES as well, like the much weaker dependence of turbulence modeling. The modeled part of the averaged (or filtered) Navier-Stokes equations are depending on an accurate description of the turbulent quantities, which in RANS modeling usually are obtained from at least two differential transport equations. As differential equations, these are completely determined by their boundary conditions. In LES, when modeling only small (more isotropic) scales of turbulence, non-differential equation models can be considered. Thus, the dependence of boundary conditions for the modeled part will vanish.

Other re-considerations which must be made are the use of steady symmetric inlet boundary conditions. In the experimental work by Dahlhaug, observations were made of an asymmetric vortex filament originating from far upstream of the diffuser, which calls for (unsteady) asymmetric inlet boundary conditions for the LES calculations.

To obtain unsteady (turbulent) inlet boundary conditions for a LES of swirling flow in a diffuser, different approaches are possible. The most obvious one is to do a LES of a swirling flow in a pipe using steady (laminar) inlet boundary conditions, but elongate the pipe far enough in the upstream direction to allow development of turbulence from numerical instabilities (i.e. transition). A disadvantage of this approach is that it is impossible to a priori make a good estimation of how far the pipe must be elongated for ‘numerical turbulence' to transform to 'real turbulence'. Geometrical and/or superimposed numerical disturbances may be a way speed up the development. Another approach is to compute the flow in a straight pipe with periodic boundary conditions in the axial direction, i.e. to use the unsteady outlet solution as the inlet solution. Results from such a computation can be used as inlet boundary conditions for diffuser computations. However, for a computation with periodic boundary conditions, some issues concerning the axial decay of swirling flow must be solved.

Appendix A

A Return to the Equations

In this appendix, some important terms of the governing equations are analyzed in order to evaluate the computed solution. Also, the analysis will serve as a step towards a better understanding of the most important features governing the turbulent swirling flow through a diffuser. The expected behavior of turbulence are discussed in the frame of the exact turbulent kinetic energy equation, the momentum equation and physical reasoning. Also included are an attempt to analytically describe the axial pressure gradient field which must be known for the possible use of periodic boundary conditions in the axial direction, as discussed in chapter 6.

A.1 The Influence of Swirl on Turbulence

To analytically deduce the effect of swirl on turbulence, the equation for the turbulent kinetic energy (equation (2.4.10)) can be transformed to a polar coordinate system by using the transformation (y,z to r,θ):

$$\begin{aligned}
v &= u_r\cos(\theta) - u_\theta\sin(\theta) \\
w &= u_r\sin(\theta) + u_\theta\cos(\theta) \\
\partial_v &= \cos(\theta)\partial_r - (\sin(\theta)/r)\partial_\theta \\
\partial_w &= \sin(\theta)\partial_r + (\cos(\theta)/r)\partial_\theta
\end{aligned} \tag{A.1.1}$$

If the axial gradients are neglected, the transformed production term of the k-equation can be expressed

$$P_k = -\frac{\overline{u_\theta^2}}{r}\partial_\theta U_\theta - \overline{u_\theta u_r}\partial_r U_\theta - \frac{\overline{u_\theta u_r}}{r}\partial_\theta U_r - \overline{u_r^2}\partial_r U_r \tag{A.1.2}$$

Assuming $U_r = 0$ and homogeneity (i.e. no mean gradients) in the azimuthal direction gives

$$P_k = -\overline{u_\theta u_r} \partial_r U_\theta \tag{A.1.3}$$

It can be deduced by looking at equation (A.1.3) that the swirl will give a positive contribution to the production of turbulent kinetic energy, since $\overline{u_\theta u_r}$ and $\partial_r (r U_\theta)$ always have the opposite signs. This can be understood by physical reasoning: A positive radial fluctuation in the boundary layer moves down the negative radial gradient of U_θ. Hence, it is carrying a larger momentum which will result in a positive tangential fluctuation. Since the co-existing fluctuations have the same sign, the correlation will be positive. Similarly, a negative radial fluctuation will correlate with a negative tangential fluctuation. A look at the radial momentum equation (see for example [9]), simplified in the same manner as above, gives another hint. The centrifugal forces are balanced by the radial pressure gradient, i e

$$\rho \frac{U_\theta^2}{r} = \partial_r P \tag{A.1.4}$$

where $\partial_r P \geq 0$ always. Further, as long as U_θ is growing in the radial direction, a positive radial fluctuation will be suppressed by the growing pressure gradient and a negative radial fluctuation will be return to the streamline it departured from, due to its higher angular velocity. Hence, radial turbulence will be damped in the forced vortex region. The experimental data by Dahlhaug [1] confirms this theory. Closer to the wall, where U_θ is dominated by the viscous boundary condition and accordingly $\partial_r (U_\theta) < 0$, a quite unstable regime is found. According to equation (A.1.4) the pressure gradient decays along with U_θ in the radial direction (see figure (A.1.1), and positive radial fluctuations will be augmented in the entire free vortex region. Of course, also the negative radial fluctuations will be augmented, but this is due to their lower angular velocity. One important thing can now be concluded; the centrifugal forces will cause a high degree of anisotropy in the forced vortex region since they only will affect radial fluctuations. This is also verified by the measured data provided by Dahlhaug, see figure 4.4.7 (b); the radial components of the fluctuations in the forced vortex region are found to be three to five times smaller than the tangential and axial components.

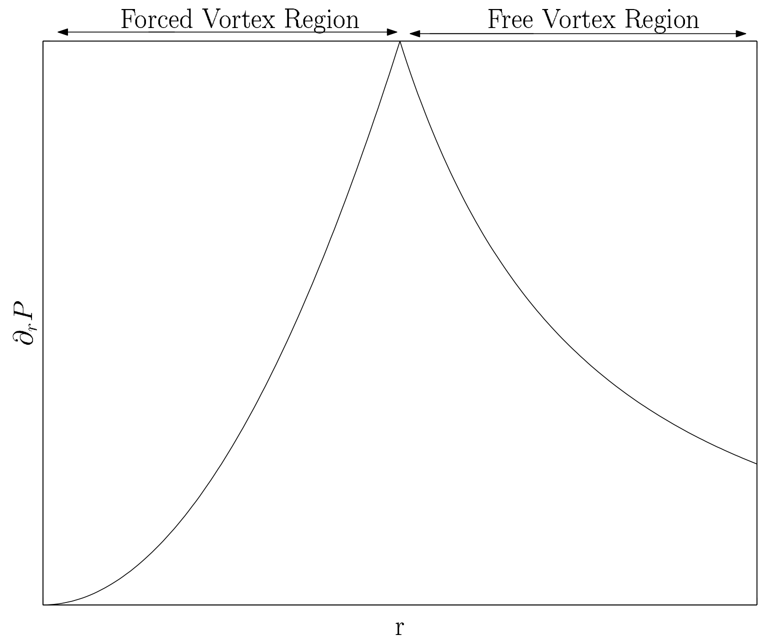

FIGURE A.1.1: A radial pressure gradient calculated from equation (A.1.4).

A.2 The Influence of the Diffuser on Turbulence

Transforming back to Cartesian coordinates and writing the equations for a 2D diffuser gives (U and x again defined in the axial direction, V and y in the wall normal direction)

$$P_k = -\overline{u^2}\partial_x U - \overline{uv}\partial_y U - \overline{uv}\partial_x V - \overline{v^2}\partial_y V \tag{A.2.5}$$

In steady 2D channel flow, all terms on the right hand side but $-\overline{uv}\partial_y U$ are zero. As soon as the flow reach the entrance of the diffuser, $\partial_x U$ and $\partial_x V$ enters the equation carrying negative values, while and $\partial_y U$ remains positive, although it will decrease in magnitude. An order of magnitude analysis gives the relation among all gradients: Let the diffuser length be L, the inlet and outlet radius be R and $2R$ respectively and let the centerline velocity be U_c

and $U_c/2$. Then, if $R \sim L/10$:

$$\begin{aligned} \partial_x U \sim \frac{U_{cl}}{2L} &< 0 \\ \partial_y U \sim \frac{5U_{cl}}{2L} &> 0 \\ \partial_x V \sim \frac{U_{cl}}{10L} &< 0 \\ \partial_y V \sim \frac{U_{cl}}{2L} &> 0 \end{aligned} \tag{A.2.6}$$

To a first order accuracy, the term including $\partial_x V$ can be neglected, being 25 times smaller than $\partial_y U$. The two normal gradients that enters the equation at the beginning of the expansion are equal in magnitude and will cancel eachother due to continuity. The significant term of shear strain remaining from the parallel flow will decrease in magnitude, but will still be the most dominant term. In the upstream parallel flow it can be approximated as $\partial_y U \sim \frac{10U_{cl}}{L}$ and the due to the expansion it will be reduced by a factor of four. It can be expected that the decrease of this term is what determines the rate of production of turbulent kinetic energy, and this can explain why there is a decay of turbulent kinetic energy during the expansion.

A.3 The Axial Pressure Gradient

By assuming that the radial gradients are much bigger than the axial gradient, an expression for the axial gradient of pressure can be found. First, by integrating equation (A.1.4), an expression for the radial distribution of pressure is found. P_c denotes the pressure along the centerline $r = 0$.

$$P(x)_{r=R} - P_{cl}(x) = \rho \int_0^R \frac{U_\theta(r,x)^2}{r}\, dr \tag{A.3.7}$$

Differentiating in the axial (x) direction gives the pressure gradient in the center of the pipe,

$$d_x P_{cl}(x) = d_x P(x)_{r=R} - \rho d_x \int_0^R \frac{U_\theta^2(r,x)}{r}\, dr \tag{A.3.8}$$

The first term on the right hand side is relatively small [12]. Due to viscous forces, the integral term in the above expression will decay in the axial direction, creating an adverse (positive) pressure gradient at the centerline. If the decay is strong enough, the flow at the centerline is completely decelerated, yielding an interior 'free' stagnation point (vortex breakdown).

Keeping the upper integral limit as an variable in equation (A.3.7), differentiating and using equation (A.3.8) gives the axial pressure gradient field.

$$\begin{aligned}\partial_x P(r,x) &= d_x P_{cl}(x) + \rho\partial_x \int_0^r \frac{U_\theta(\tilde{r},x)^2}{r}\,d\tilde{r}\\ &= d_x P(x)_{r=R} - \rho\partial_x \int_r^R \frac{U_\theta^2(\tilde{r},x)}{\tilde{r}}\,d\tilde{r}\end{aligned} \tag{A.3.9}$$

If the decay of swirl velocity is negligible the axial pressure gradient field can be approximated with the gradient of the wall pressure, or the gradient of any pressure along the radial axis, since all radial dependence will vanish. The force of the axial pressure gradient will be balanced by the wall shear stress. This fact can be used for deriving the source term in the axial momentum equation needed for driving swirling flow between periodic boundary conditions, see chapter 6.

Appendix B

Some Notes on Averaging

In this chapter, some different kinds of averaging of the Navier-Stokes equations are presented. The implications of the use of standard turbulence models in unsteady calculations are discussed, i.e. the contradicton that the URANS equations (together with the standard turbulence models) would resolve large turbulent structures.

B.1 Why Average?

The main reason for the need of averaging (and consequently the need of turbulence modeling) is the limited capacity of computers. The numerical methods[1] for solving PDE:s in use today depend on resolving all significant scales involved in the problem. To resolve all scales, i.e. to perform a direct numerical simulation (DNS) of a real industrial turbulent flow, is beyond the scope of any supercomputer today. Instead, different averaging methods are introduced, all giving - in spite of the similarities of the equations - different unknowns. Depending on the nature of the averaging, the solution to the average equations must be interpreted accordingly. Thus it is important to get an understanding of the nature of averaging. In section B.2 some aspects of the different kind of averaging are discussed.

B.1.1 Physical Instability - Numerical Stability

A non-linear problem must be solved iteratively. Numerically the problem in trying to solve the not fully resolved Navier-Stokes equations appears as instabilities during the iterations. The instabilities, given a numerical resolution, grow worse with increasing Reynolds number. This can be understood by looking at the non-dimensionalized[2] equations, equation (B.1.1), where the stabilizing viscous diffusion term goes to zero in the limit of infinite Reynolds number.

---

[1] Finite elements, volumes or differences.

$$D_0 u_i = -\frac{1}{\rho}\partial_i p + \frac{1}{Re}\partial_j \partial_j u_i \tag{B.1.1}$$

Though the diffusion term might be numerically stiff, it will always act as a *smoother* to the solution. In the averaged (volume, ensemble or time averaged) equations, the modeled unknown quantities can always be put inside the diffusion term, see equation (2.2.7), where they are allowed to grow with increasing Reynolds number, amplifying the importance of the term. Instead of making the momentum equations unstable, the effect of the modeled turbulence is the opposite.

B.2 Aspects of Averaging

The only alternative to DNS is to solve an averaged problem. There are quite a few different kinds of averaging methods of the governing equations in use today. In the following sections, the most common averaged equations are discussed.

B.2.1 RANS

RANS modeling are based on solving the Reynolds averaged Navier-Stokes equations, equation (2.2.7), and different types of closure models are used for the Reynolds stress tensor. These equations can be solved in 1D or 2D, and are the least demanding of all equations for turbulent flow. Still, the production of turbulent kinetic energy is depending of the mean flow gradient, which can be seen from equation (2.4.10). This means that even though the RANS equations do not depend on resolving turbulent structures, the gradient of the mean flow must still be accurately resolved. In the CFD community the RANS equations are usually synonymous to time averaged equations, and subsequently only applied to steady flow.

---

[2] The equation is derived using significant length and velocity scales.

B.2.2 URANS

Often, the unsteady RANS (URANS) equations are derived by a very special kind of 'time' averaging,

$$U_i(\mathbf{x}) = \overline{u_i(\mathbf{x}, t)} = \frac{1}{T}\int_{-T/2}^{T/2} u_i(\mathbf{x}, \tau)\, d\tau \tag{B.2.2}$$

As can be seen, the function U_i is no longer a function of time. To keep the mean time derivative in the 'time' averaged equations one must assume that there is a separation between the mean and turbulent scales.

$$\begin{aligned}\frac{1}{T}\int_{t}^{t+T} & \partial_0 \left(U_i(\mathbf{x}, \tau) + u_i'(\mathbf{x}, \tau)\right) d\tau \\ &= \frac{U_i(\mathbf{x}, t+T) + u_i'(\mathbf{x}, t+T)}{T} - \frac{U_i(\mathbf{x}, t) + u_i'(\mathbf{x}, t)}{T}\end{aligned} \tag{B.2.3}$$

In the limit $T \rightarrow 0$ this is *not* equal to the time derivative for the 'mean' flow, but if the assumption that the mean scales are much slower than the turbulent scales is valid, the differencing (and also averaging) time may not have to be drawn to the limit. Instead it can be drawn to an arbitrary value in the region between the turbulent and the mean scales, or ideally to the sum of a sufficient many integral time scales. There is no way to make an accurate estimate of where this region is situated. Also, most numerical methods demands a timestep common to the entire computational domain. In order to allow the ratio of mean and turbulent scales to vary at walls and in free shear layers, there must be a very large separation of the scales to assure that the averaging time is sufficient. However, given weakly time dependent boundary conditions for the mean quantities, the timestep may be chosen big enough.

Since there is usually no large separation between mean and turbulent scales, turbulent structures are thought to end up in the solution of the URANS equations. If the solution to the URANS equations would contain turbulent structures; do the standard turbulence models get information of what is resolved or do they still model *all* turbulence? As noted by Menter [6], no information of what is resolved is transfered to the model. The only feedback the model achieve is the resolved gradients, which in case of resolved large turbulent structures usually will be greater than the mean gradients. This may, as also will be discussed in appendix C.4, lead to overestimated modeled quantities and can explain why the standard models are considered too dissipative for unsteady flow. As an example: If the mean gradient of an URANS calculation is exchanged to a gradient containing resolved turbulent structures it will be less smooth. Since the turbulence models usually are insensitive to the sign of the gradient; the more turbulence that is resolved, the more will be modeled. This is contradictory and may be one of the reasons why the two-equation models tends to damp all expected unsteadiness of an URANS calculation. If k is overpredicted, so is the turbulent viscosity, and the diffusion term of the URANS equation (equation (2.2.7)) will be far too large, resulting in a smoothed solution. The computation will probably end up as the steady solution of the time averaged equations.

B.2.3 The Ensemble Average and the Randomness of Turbulence

One way to avoid the assumptions of above is to use the ensemble averaged equations. These are identical to the URANS equations, but here the unknown function U denotes the average of an *infinite* number of realizations. They are extensively used by theoreticians. By definition, the solution cannot be random, since the ensemble average equals an arithmetic mean that is drawn to its limit. The randomness of the arithmetic mean will by definition vanish in the limit. If turbulence were *random* fluctuations, the ensemble averaged equations would not resolve any turbulence. Equivalently, if URANS do resolve large unsteady structures, they may not be considered random. Further, since all the turbulence is enclosed in the Reynolds stress tensor τ_{ij}, the solution obtained from a calculation of the ensemble averaged equations would not contain turbulent structures. Still there is one problem of solving the ensemble averaged equations, and that is to design a problem without any disturbances. As the boundary conditions accordingly must be regarded as ensemble averaged, they should not contain anything that might distort the flow. In the case of symmetrical geometries, the level of symmetry needed is almost impossible to obtain.

B.2.4 Filtered Functions and the LES

In this section there will be no distinct separation between mean and turbulent scales, instead they will be referred to as resolved and unresolved scales of unsteady motion. The idea about filtering is to obtain and solve for a function much smoother than the exact solution. A ‘smoothed’ function will not have to be resolved to the same extent as the original. One way of smoothing is to apply a *filter*. Filtering is more general way of averaging than the ‘time’ average of above. A time filter defined as in equation (2.5.14) yields a function which is still dependent of time. The assumption of a scale-separation is now superfluous since the filtered function is dependent of all time, i.e. it can be drawn to the limit $T \to 0$ where the function resembles itself. Numerically, given a finite time step, fast fluctuations will not be resolved and a *substep model* must be used. Slower timescales will be part of the solution. A necessary condition for this is of course that the spatial resolution correlates with the resolved timescales, since what is not resolved spatially neither can be viewed in time. In practice numerical stability requires very small timesteps, why it is in practice the spatial resolution that determines the solution. The corresponding spatial filtering can be defined as in equation (2.5.15), and this is the most obvious and common filter for LES. The part of u_i that is not resolved is referred to as the *subgrid* part, since usually the resolution of the computational mesh implicitly defines the width of the spatial filter.

Some important properties of filtering will affect the governing equations. Applying the filter twice yields a new unknown, and filtering the subgrid part yields not zero, see section 2.5. Subsequently, the filtered equations of motion will differ from the URANS equations. Using equation (2.5.18), turbulence modelers will only have to consider modeling the subgrid scales of turbulence. Ironically, the equations resulting from filtering the Navier-Stokes equations are identical to the URANS equations, with the form of the term τ_{ij} being the only exception. LES is always run in 3D space and time, since turbulence is always three dimensional and unsteady. Otherwise, the only difference between LES and URANS is - if one for a moment forget about the underlying assumptions in their derivations - the choice of turbulence model [6].

Appendix C

The Most Common Turbulence Models

To model correlations of velocities, there is a need for a length and a time scale at every point in the domain. The *two-equation* models are the simplest candidates for solving this problem, even though there are *one-equation* models where the length scale is obtained from an algebraic relationship or the grid, like in the case of the Smagorinsky model. The internal relation between the velocity correlations are most often set by the Boussinesq assumption, equation (C.1.6). More complex models include the $v^2 - f$ model (four equations) and the Reynolds stress model (six equations). In this appendix the most commonly used turbulence models are described. Some implications of the two-equation models are discussed, especially the Boussinesq assumption.

C.1 The $k - \varepsilon$ Model

The standard $k - \varepsilon$ model is widely used, mostly because of its robustness in performance. It is a two-equation model depending on the Boussinesq assumption, equation (C.1.6), for the modeling of P_k, equation (2.4.11). The exact ε-equation can be derived from the Navier-Stokes equations, but due to the many unknowns introduced by the derivation it is never used in turbulence modeling. Instead a simplified equation for ε is invented and solved, see equation (C.1.4).

Below the complete $k - \varepsilon$ model is shown. The k-equation is written as

$$\partial_0 k + U_j \partial_j k = P_k^{model} + D_k^{model} - \varepsilon \tag{C.1.1}$$

where

$$\begin{aligned} P_k^{model} &= 2\nu_t S_{ij}\partial_j U_i && \text{(C.1.2)} \\ D_k^{model} &= \partial_j(\nu + \frac{\nu_t}{\sigma_k}\partial_j k) && \text{(C.1.3)} \end{aligned}$$

and the ε-equation

$$\partial_0\varepsilon + U_j\partial_j\varepsilon = \frac{\varepsilon}{k}\left(C_{\varepsilon 1}P_k^{model} - C_{\varepsilon 2}\varepsilon\right) + \partial_j\left((\nu + \nu_t/\sigma_\varepsilon)\partial_j\varepsilon)\right) \qquad \text{(C.1.4)}$$

The coefficients are usually obtaining the values

$$\begin{aligned} C_{\varepsilon 1} &= 1.44 \\ C_{\varepsilon 2} &= 1.92 \\ C_\mu &= 0.09 && \text{(C.1.5)} \\ \sigma_k &= 1.0 \\ \sigma_\varepsilon &= 1.3 \end{aligned}$$

The connection to the Reynolds averaged Navier-Stokes equations (equation (2.2.7)) are through the Boussinesq assumption:

$$-u_i u_j = 2\nu_t S_{ij} - \frac{2}{3}k\delta_{ij} \qquad \text{(C.1.6)}$$

where ν_t is defined as

$$\nu_t = C_\mu k^2/\varepsilon \qquad \text{(C.1.7)}$$

C.2 The $k - \omega$ Model

The first $k - \omega$ model was proposed by Kolmogorov as early as 1942. It has evolved during the last decades and presented below is the version of Wilcox 1988 [16]. The $k - \omega$ model resembles most of the $k - \varepsilon$ model and ε is related to ω by

$$\varepsilon = \beta^*\omega k \qquad \text{(C.2.8)}$$

The complete $k - \omega$-equation is given as

$$\begin{aligned} \partial_0 k + U_j\partial_j k &= P_k^{model} + D_k^{model} - \beta^*\omega k \\ \partial_0\omega + U_j\partial_j\omega &= \partial_j\left((\nu + \nu_t/\sigma_\omega)\partial_j\omega\right) - \frac{\omega}{k}(c_{\omega 1}P_k^{model} + c_{\omega 2}k\omega) \\ P_k^{model} &= 2\nu_t S_{ij}\partial_j U_i && \text{(C.2.9)} \\ D_k^{model} &= \partial_j\left((\nu + \nu_t/\sigma_k)\partial_j k\right) \\ \nu_t &= k/\omega \end{aligned}$$

where the closure coefficients are

$$\beta = 0.09,\ c_{\omega 1} = 5/9,\ c_{\omega 2} = 3/40,\ \sigma_k = \sigma_\omega = 2 \tag{C.2.10}$$

C.3 The Reynolds Stress Model

The dependence of an eddy viscosity is avoided in the Reynolds stress model, where a transport equation for each Reynolds stress is modeled. The model is based on equation (2.3.9). One of the biggest advantages of this model is that the there are no need to model the production terms. It also has the potential to predict anisotropic properties of turbulence, and account for effects of flow history. The only drawback is that the model is usually considered far too unstable numerically. There are three terms in equation (2.3.9) that must be modeled, ε_{ij}, Π_{ij} and C_{ijk}. The standard model by Launder-Reece-Rodi is shown below.

$$\partial_0\tau_{ij} + U_k\partial_k\tau_{ij} = P_{ij} - \Pi_{ij} + \partial_k\left(\nu\partial_k\tau ij + C_{ijk}\right) + \varepsilon_{ij} \tag{C.3.11}$$

The dissipation is modeled as:

$$\partial_0\varepsilon + U_j\partial_j\varepsilon = \frac{\varepsilon}{k}\left(C_{\varepsilon 1}\tau_{ij}\partial_j U_i - C_{\varepsilon 2}\varepsilon\right) - C_\varepsilon\partial_j\left(\frac{k}{\varepsilon}\tau_{km}\partial_m\varepsilon\right) \tag{C.3.12}$$

$$\varepsilon_{ij} = \frac{2}{3}\varepsilon\delta_{ij} \tag{C.3.13}$$

The pressure strain model is

$$\begin{aligned}\Pi_{ij} = C_1\frac{\varepsilon}{k}\left(\tau_{ij} + \frac{2}{3}k\delta_{ij}\right) - \hat{\alpha}\left(P_{ij} - \frac{2}{3}P\delta_{ij}\right) - \\ \hat{\beta}\left(D_{ij} - \frac{2}{3}P\delta_{ij}\right) - \hat{\gamma}k\left(S_{ij} - \frac{1}{3}S_{kk}\delta_{ij}\right) + \\ \frac{k^{3/2}}{\varepsilon\, n}\left[0.125\frac{\varepsilon}{k}\left(\tau_{ij} + \frac{2}{3}k\delta_{ij}\right) - 0.015\left(P_{ij} - D_{ij}\right)\right]\end{aligned} \tag{C.3.14}$$

The models for the convection and the diffusion are

$$C_{ijk} = \frac{2}{3}C_s\frac{k^2}{\varepsilon}\left(\partial_i\tau_{jk} + \partial_j\tau_{ik} + \partial_k\tau_{ij}\right) \tag{C.3.15}$$

$$D_{ij} = \tau_{ik}\partial_j U_k + \tau_{jk}\partial_i U_k \tag{C.3.16}$$

The model coefficients are

$$\begin{aligned}
\hat{\alpha} &= (8 + C_2)/11 \\
\hat{\beta} &= (8C_2 - 2)/11 \\
\hat{\gamma} &= (60C_2 - 4)/55 \\
C_1 &= 1.8 \\
C_2 &= 0.6 \\
C_s &= 0.11 \\
C_\varepsilon &= 0.18 \\
C_{\varepsilon 1} &= 0.44 \\
C_{\varepsilon 2} &= 1.9
\end{aligned} \tag{C.3.17}$$

For modeling of subgrid stresses, equation (2.5.19) in LES, the most popular choice is the Smagorinsky model. It is a simple one-equation model, based on the assumption that the not resolved local turbulent length scale is proportional to the size of the local computational cell (Δ).

$$\tau_{ij} = 2\nu_t S_{ij} \tag{C.3.18}$$

$$\nu_t = (C_s \Delta)^2 \sqrt{S_{ij} S_{ij}} \tag{C.3.19}$$

The modeled τ_{ij} are directly inserted in the governing (LES) equation.

C.4 Limitations of the Boussinesq Assumption

The Boussinesq assumption introduces an isotropic eddy viscosity ν_t, which is used in all two-equation models. By dimensional analysis, it can be defined as

$$\nu_t = C_\mu k^2/\varepsilon \tag{C.4.20}$$

if it is only depending on local turbulent quantities. The coefficient C_μ is usually set to the constant value of 0.09.

The assumption of an isotropic[1] eddy viscosity do not seem to apply to swirling flow. Radial turbulence is damped by centrifugal forces, and especially the tangential stress component is expected to be amplified due to streamline curvature. Also, flow-history effects on the Reynolds stresses can persist for a long distance, which makes the linear relationship between $u_i u_j$ and S_{ij} even more doubtful [16]. A look at the Reynolds stress equation (2.3.9), immediately tells us that the Reynolds stress is subject to be convected in space.

---

[1] Invariant of direction.

There are other limitations of the Boussinesq assumption as well. Substitution of the Reynolds stress tensor in the production term of the equation of turbulent kinetic energy, equation (2.4.11), yields

$$P_k^{model} = 2\nu_t S_{ij} \partial_j U_i \tag{C.4.21}$$

It follows from the definitions that the production term (P_k), modeled by using Boussinesq assumption has limited ability to predict detailed physics of a non-parallel flow. As soon as a positive normal strain[2] is introduced in the flow, the exact production term P_k, defined in equation (2.4.11), will get a negative contribution. The modeled production term, equation (C.1.3), will on the other hand obtain a positive value. This may lead to overpredicted turbulent quantities. This is one of the reasons why standard $k-\varepsilon$ and $k-\omega$ models must be used with caution when modeling non-parallel turbulent flow. Moreover, if the mean gradient is exchanged to a gradient containing resolved turbulent structures (like the solution of an URANS equation) it will be less smooth. Since the model is insensitive to the sign of the gradient; the more turbulence is resolved, the more will be modeled. This is contradictory and may be one of the reasons that the two-equation models tends to damp all expected unsteadiness of an URANS calculation. If k is overpredicted, so is the turbulent viscosity, and the diffusion term of the URANS equation (equation (2.2.7)) will be far too large, resulting in a smoothed solution. In fact, it will end up in the steady solution of the time averaged equations.

---

[2] $\partial_i u_i > 0$, i = 1,2 or 3, no summation over i.

Bibliography

[1] O. G. Dahlhaug: *A study of swirl flow in draft tubes,* Ph.D. thesis 1997:30, Institutt for termisk energi og vannkraft, NTNU Trondheim, Norway, 1997.

[2] S. L. Dixon: *Fluid mechanics and thermodynamics of turbomachinery, 4th ed.,* Butterworth-Heinemann, Woburn MA, USA, 1998.

[3] J. P. Van Doormaal and G. D. Raithby: *Enhancements of the SIMPLE method for predicting incompressible fluid flows,* Numerical Heat Transfer, 7:147-163, 1984.

[4] J. H. Faler and S. Leibovich: *An experimental map of the internal structure of a vortex breakdown,* Journal of Fluid Mechanics, Vol. 86, 2:313-335, 1978.

[5] A. H. Hirsa, J. M. Lopez and R. Miraghaie: *Symmetry breaking to a rotating wave in a lid-driven cylinder with a free surface: Experimental observation,* Physics of Fluids, Vol. 14, 6 (Letters section), 2002.

[6] F. R. Menter, M. Kuntz and R. Bender: *A Scale Adaptive Simulation Model for Turbulent Flow Predictions,* 41st Aerospace Science Meeting and Exhibit, 6-9 Jan 2003, Reno NA, USA, AIAA 2003-0767.

[7] H. Nilsson and L. Davidsson: *CALC-PVM: A parallel SIMPLEC multiblock solver for turbulent flow in complex domains,* Internal report 98/12, Division of Thermo and Fluid Dynamics, Chalmers University of Technology, Göteborg, Sweden, 1998.

[8] H. Nilsson: *Numerical Investigations of Turbulent Flow in Water Turbines,* Ph. D. thesis, Division of Thermo and Fluid Dynamics, Chalmers University of Technology, Göteborg, Sweden, 2002.

[9] R. L. Panton: *Incompressible Flow,* John Wiley & Sons Inc., New York NY, USA, 1996.

[10] A. Ruprecht, T. Helmrich, T. Aschenbrenner and T. Scherer: *Simulation of Vortex Rope in a Turbine Draft Tube,* Proceedings of the 21st IAHR Symposium, Hydraulic Machinery and Systems, Vol. 1, 259-266, Lausanne, Switzerland, 2002.

[11] C. J. Scott and K. W. Bartlett: *Decaying Annular Swirl Flow with Inlet Solid Body Rotation,* Journal of Fluids Engineering, Vol. 98, Series 1, 1:33-40, 1976.

[12] D. G. Sloan, P. J. Smith and L. D. Smoot: *Modeling of swirl in turbulent flow systems,* Prog. Energy Combust. Sci., Vol. 12, 163-250, 1986.

[13] F. Sotiropoulos and Y. Ventikos: *The three-dimensional structure of confined swirling flows with vortex breakdown,* Journal of Fluid Mech, Vol. 426, 155-175, 2000.

[14] A. Spohn, M. Mory and E. J. Hopfinger: *Experiments on vortex breakdown in a confined flow generated by a rotating disc,* Journal of Fluid Mech, Vol. 98, 73-99, 1998.

[15] F. M. White: *Fluid Mechanics,* McGraw-Hill, USA, 1999.

[16] D. C. Wilcox: *Turbulence Modeling for CFD, 2nd ed.* DCW Industries Inc., La Cañada CA, USA, 2002.